Long lifetime and selective accumulation of the A-type lamins accounts for the tissue specificity of Hutchinson-Gilford progeria syndrome

Authors: John Hasper[1], Kevin Welle[2], Kyle Swovick[2], Jennifer Hryhorenko[2], Sina Ghaemmaghami[2,3], Abigail Buchwalter[1,4,5*]

Affiliations:

[1]Cardiovascular Research Institute, University of California, San Francisco, San Francisco, CA
[2]University of Rochester Mass Spectrometry Resource Laboratory, Rochester, NY
[3]Department of Biology, University of Rochester, Rochester, NY
[4]Department of Physiology, University of California, San Francisco, San Francisco, CA
[5]Chan Zuckerberg Biohub, San Francisco, CA
*corresponding author. email: Abigail.buchwalter@ucsf.edu

Author Contributions: J. Hasper performed in vivo labeling experiments, tissue isolations, protein and DNA extractions, and protein biochemistry experiments with assistance from A.B. J. Hryhorenko, K.W. and K.S. prepared and ran samples for LC-MS/MS. A.B., J. Hasper, K.W., K.S., and S.G. analyzed data. A.B. prepared the figures and wrote the manuscript.

Competing Interest Statement: the authors have no competing interests to report.

Classification: Biological Sciences / Cell Biology

Keywords progeria / nuclear lamina / protein homeostasis

This PDF file includes:

Main Text
Figures 1 to 7
Table 1

Abstract

Mutations to the *LMNA* gene cause laminopathies including Hutchinson-Gilford progeria syndrome (HGPS) that severely affect the cardiovascular system. The origins of tissue specificity in these diseases are unclear, as the A-type Lamins are abundant and broadly expressed proteins. We show that A-type Lamin protein and transcript levels are uncorrelated across tissues. As protein-transcript discordance can be caused by variations in protein lifetime, we applied quantitative proteomics to profile protein turnover rates in healthy and progeroid tissues. We discover that tissue context and disease mutation each influence A-type Lamin protein lifetime. Lamin A/C has a weeks-long lifetime in the aorta, heart, and fat, where progeroid pathology is apparent, but a days-long lifetime in the liver and gastrointestinal tract, which are spared from disease. The A-type Lamins are insoluble and densely bundled in cardiovascular tissues, which may present an energetic barrier to degradation and promote long protein lifetime. Progerin is even more long-lived than Lamin A/C in the cardiovascular system and accumulates there over time. Progerin accumulation interferes broadly with protein homeostasis, as hundreds of abundant proteins turn over more slowly in progeroid tissues. These findings indicate that potential gene therapy interventions for HGPS will have significant latency and limited potency in disrupting the long-lived Progerin protein. Finally, we reveal that human disease alleles are significantly over-represented in the long-lived proteome, indicating that long protein lifetime may influence disease pathology and present a significant barrier to gene therapies for numerous human diseases.

Significance statement (50-120 words)

Many human diseases are caused by mutations to broadly expressed proteins, yet disease mysteriously manifests only in specific tissues. An example of this is Hutchinson-Gilford progeria syndrome (HGPS), which is caused by a mutation to the Lamin A/C protein. We show that this mutation slows the turnover of Lamin A/C proteins in disease-afflicted tissues, causing the mutant “Progerin” protein to accumulate over time and interfere with the normal turnover of hundreds of other proteins. Because Progerin is a long-lived protein, effective therapies for this disease will need to attack the protein and not just the gene that encodes it.

Main Text

Introduction

The nuclear lamina is an intermediate filament meshwork that underlies the nuclear envelope. In mammals, this structure is composed of two classes of Lamin proteins: the “A-type” lamins (Lamins A and C), and the “B-type” lamins (Lamins B1 and B2). Lamins assemble into bundled filaments that strengthen the nucleus and scaffold the genome.

The *LMNA* locus encodes the Lamin A and C proteins and is a hotspot for disease-linked mutations; hundreds of mutations to *LMNA* have been linked to at least 15 distinct syndromes, collectively referred to as “laminopathies”(*1*). While the Lamin A/C proteins are broadly expressed, laminopathies primarily afflict the cardiovascular system, muscle, bone, and fat(*1*). Hutchinson-Gilford progeria syndrome (HGPS) is a rare and devastating autosomal dominant laminopathy that resembles physiological aging at an accelerated rate, with rapid deterioration of the skin, adipose tissue, and cardiovascular system. Most cases of HGPS are caused by a single base pair substitution (GGC > GGT) that activates a cryptic splice site, resulting in the in-frame deletion of a portion of exon 11 in *LMNA* and the production of a toxic, dominant negative “Progerin” protein.

Several gene therapy approaches have recently been tested in mouse models of HGPS, ranging from disrupting the mutant allele with CRISPR/Cas9 indels(*2*, *3*), correcting the mutant allele with base editing(*4*), or interfering with the unique RNA splicing event that produces the *Progerin* transcript(*5*–*8*). Because HGPS is caused by the toxic effects of a dominant negative protein, an effective gene therapy will need to induce the removal and replacement of as much of the Progerin protein as possible. However, recent work indicates that gene therapies have variable effects on Progerin protein levels *in vivo*; for instance, in various treatment regimes that effectively clear the mutant protein from the liver, the protein persists to some extent in the cardiovascular system (*3*–*6*, *8*, *9*). In one particularly striking case, high levels of Progerin were found to persist in the cardiovascular system after over 5 months of treatment with splice-interfering antisense oligonucleotides, long after effective depletion of the *Progerin* transcript had been achieved (*6*). Altogether, these findings indicate that removing Progerin protein is a major bottleneck that may limit the potency of HGPS gene therapies.

Why is Progerin so intractable to removal in the cardiovascular system? Progerin could be produced in particularly high amounts in cardiovascular tissues, which are known to express high levels of Lamin A/C(*10*). A second, non-exclusive possibility is that Progerin is especially

99 long-lived in the cardiovascular system. Notably, the closely related B-type Lamin proteins have
100 extremely long lifetimes of months to years in the murine nervous system(*11*, *12*). The lifetimes
101 of the A-type Lamins within tissues have not been defined. We previously profiled protein lifetimes
102 in cultured progeroid fibroblasts and found no evidence that the HGPS-causative mutation impairs
103 the turnover of Lamin A/C(*13*). However, these experiments could not address the potential
104 influence of tissue context on the turnover rate of Lamin A/C and/or Progerin.
105 Here, we deploy our recently developed dynamic proteomic approach, turnover and
106 replication analysis by isotope labeling (TRAIL)(*14*) to define the turnover rate of the Lamin A/C
107 and Progerin proteins within tissues of healthy and progeroid mice. We report that Lamin A/C
108 turns over an order of magnitude more slowly within disease-afflicted tissues compared to
109 disease-spared tissues. Further, we show that the Progerin mutant is even more long-lived than
110 wild-type Lamin A/C in the cardiovascular system, leading us to estimate a months-long lifetime
111 of this toxic mutant protein in these diseased tissues. In contrast, we show that protein abundance
112 does not correlate with disease susceptibility in human or mouse tissues. By evaluating the
113 incidence of human disease alleles across protein turnover deciles, we reveal that human disease
114 alleles are generally over-represented in the long-lived proteome. These findings have major
115 implications for both the pathogenesis and treatment of laminopathies and establish a novel
116 paradigm for rare human diseases caused by the action of long-lived mutant proteins.
117
118 **Results**
119
120 ***High abundance of Lamin A/C/Progerin proteins is not restricted to cardiovascular tissues***
121
122 High Progerin abundance could both drive disease and thwart gene therapies. We
123 reasoned that tissues that express high levels of Lamin A/C in healthy individuals may also
124 express more Progerin in diseased individuals, and we mined a quantitative proteomic atlas of 29
125 human tissues(*15*) to systematically evaluate the relationship between Lamin A/C protein
126 expression and laminopathy pathology. This tissue proteome atlas relies on intensity-based
127 absolute quantification (iBAQ) to accurately quantify protein abundance(*16*) and on the histone-
128 based "proteomic ruler" approach(*17*) to estimate protein copy numbers per cell. These data
129 indicate that the human Lamin A/C proteins are extremely abundant in smooth muscle (Fig. 1A),
130 consistent with previous reports in mouse tissues(*18*, *19*). Because vascular smooth muscle is
131 prominently affected in *LMNA*-linked Hutchinson-Gilford progeria syndrome(*20*, *21*), these data
132 could suggest that high Lamin A/C abundance correlates with disease vulnerability. However, the

133 heart and adipose tissue are also afflicted in HGPS and other laminopathies, but these tissues
134 express Lamin A/C at a level comparable to many unaffected human tissues (Fig. 1A). In fact,
135 26/29 of the analyzed tissues are estimated to produce more than 10^7 copies of Lamin A/C per

Figure 1.

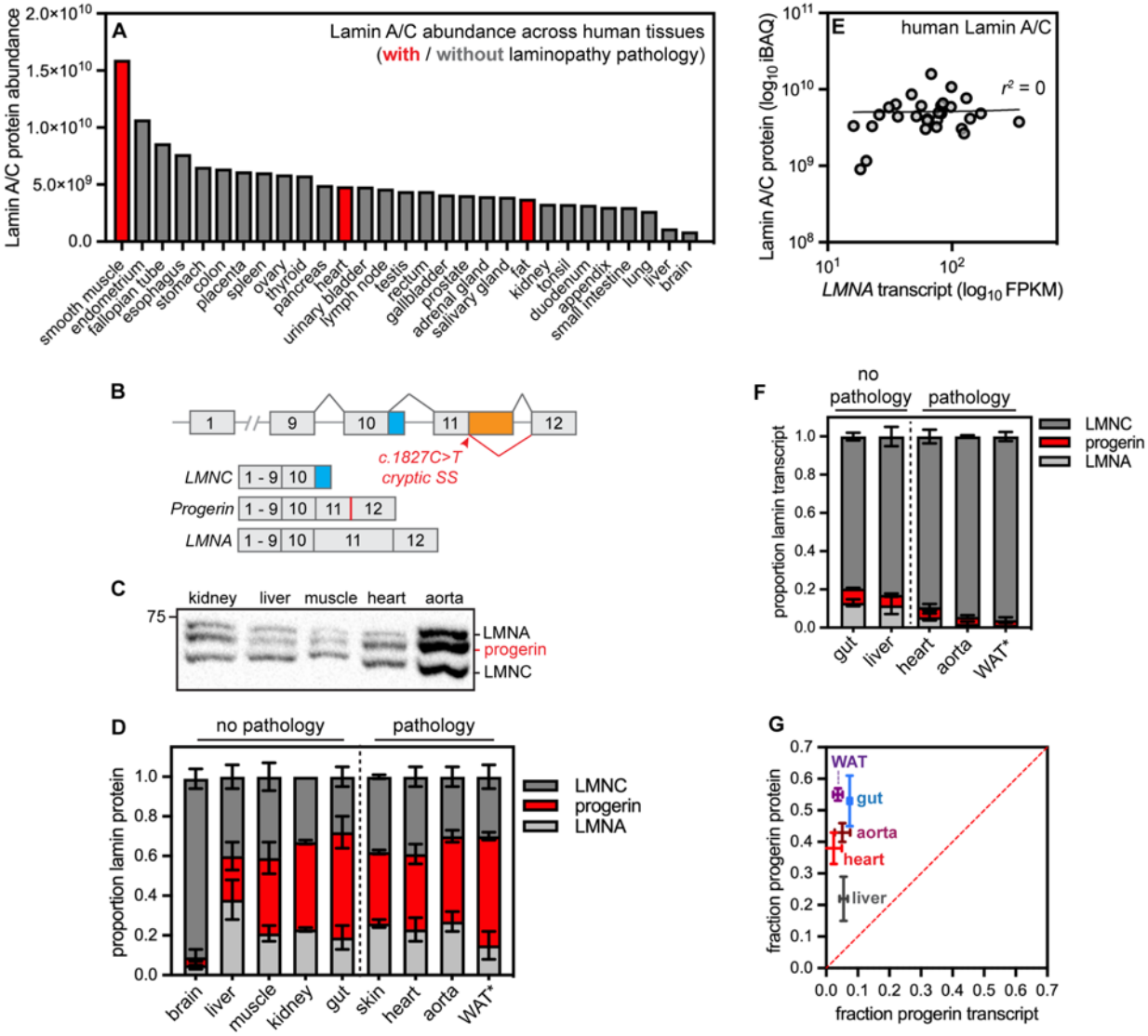

Figure 1. Poor correlation between trasncript and protein abundance for the long-lived disease-linked protein Lamin A/C. (A) iBAQ quantification of Lamin A/C absolute protein abundance across 29 human tissues. Data reanalyzed from Wang et al., *Mol Syst Biol* 2019. (B) Diagram of the *LMNA* locus, which produces the *LMNA* (exons 1-12) and *LMNC* (exons 1-10) transcripts. In HGPS, a base pair substitution activates a cryptic splice site, leading to the production of the toxic *Progerin* transcript that contains an in-frame deletion in exon 11. (C) Representative Western blot of tissue extracts from 9-month old $LMNA^{G609G/+}$ mice. 20 ug of protein loaded per lane. (D) Quantification of proportional Lamin A, Lamin C, and Progerin protein isoform abundance by Western blotting and densitometry in 9-month old $LMNA^{G609G/+}$ mice. *indicates that WAT was analyzed from 3-month-old animals because of the rapidly progressing lipodystrophy in these mice. (E) Lamin A/C absolute protein abundance (iBAQ) and *LMNA* RNA abundance (RNAseq FPKM) are very poorly correlated ($r^2 = 0$) across 29 human tissues. Data reanalyzed from Wang et al., *Mol Syst Biol* 2019. (F) Proportional abundance of *LMNA, LMNC*, and *Progerin* transcript abundance determined by digital droplet PCR in tissues from 9-month old $LMNA^{G609G/+}$ mice. *indicates that WAT was analyzed from 3-month-old animals. (G) Proportional abundance of *Progerin* transcript
136 and Progerin protein are very poorly correlated across tissues from $LMNA^{G609G/+}$ mice.

137 cell (Fig. S1A), indicating that high expression levels of Lamin A/C are not sufficient to drive
138 disease.

139 The abundance ratio of the A-type (Lamin A/C) to B-type (Lamin B1 and B2) lamins
140 influences nuclear mechanics(*18*) and it has been proposed that tissues with a high ratio of A-
141 type:B-type lamins might be most sensitive to *LMNA* mutations(*19*). Consistent with previous
142 analyses in the mouse(*19*), the ratio of A-type:B-type lamins is very high in the human heart
143 (8.6:1), smooth muscle (7.2:1), and fat (4.3:1) which are especially vulnerable to *LMNA* mutations
144 (Fig. S1D). However, this ratio is also comparably high in many unaffected tissues (Fig. S1D).
145 Therefore, a high ratio of A-type to B-type Lamins is not sufficient to drive HGPS.

146 We next considered the alternative possibility that Progerin abundance varies
147 independently of Lamin A/C abundance across diseased tissues. The genetic lesion that causes
148 HGPS activates a cryptic splice site, resulting in the in-frame deletion of a portion of exon 11 in
149 *LMNA* without altering the shorter *LMNC* isoform (Fig. 1B). This splice site operates with
150 incomplete efficiency, such that both *Progerin* and wild type *LMNA* transcripts can be produced
151 from the mutant allele; variable splice site use could thus modulate *Progerin* production across
152 tissues(*22*). To explore this possibility, we turned to a genetically modified mouse model that
153 harbors the HGPS-causative C>T substitution in the endogenous mouse *LMNA* locus
154 ($LMNA^{G609G/+}$)(*5*).

155 We evaluated the proportional abundance of the Lamin A, Lamin C, and Progerin proteins
156 by Western blotting across tissues in wild type (Fig. S2) and progeroid mice (Fig. 1C-D) by
157 detection with an antibody that detects an epitope shared across all A-type lamins (see Methods).
158 We reasoned that this approach was the most relevant way to quantify the dose of the toxic
159 Progerin protein, as the ratio of Progerin to other wild type Lamin isoforms has been proposed to
160 influence pathology(*19*). We found that Progerin contributes significantly to the total amount of A-
161 type Lamins detected in many tissues - up to 50% in some cases(Fig. 1C-D). Puzzlingly, however,
162 the proportional abundance of Progerin does not correlate with HGPS pathology; the disease
163 variant is highly abundant in afflicted tissues, such as the aorta and adipose tissue, as well as in
164 tissues that remain functional, such as the kidney and large intestine. Altogether, these analyses
165 indicate that protein abundance alone cannot explain either the vulnerability of specific tissues to
166 *LMNA* mutations or the resistance of Progerin to therapeutic interventions.

167

168 ***Lamin A/C/Progerin protein and transcript levels are very poorly correlated across tissues***

169

170 What other factors could modulate both the responsiveness of Progerin to treatment and
171 the effects of Progerin on a tissue? One potential influence could be the lifetime of the Lamin
172 A/C/Progerin proteins. A protein's lifetime reflects its rates of synthesis and degradation; short-
173 lived proteins are frequently renewed, while long-lived proteins can persist for weeks or even
174 months within mammalian tissues(*11*). Because long-lived proteins are rarely synthesized and
175 rarely degraded, their abundance may be poorly sensitive to changes in their transcript levels. To
176 explore the relationship between *LMNA* transcript and Lamin A/C protein abundance, we
177 compared tissue-matched RNAseq and proteomic data across 29 human tissues(*15*). This
178 analysis revealed that *LMNA* transcript and Lamin A/C protein abundances are uncorrelated (Fig.
179 1E, $r^2 \sim 0$). For comparison, the enzyme SYK has a high correlation between transcript and protein
180 levels across tissues(*15*) (Fig. S3, $r^2 = 0.89$). We next used digital droplet PCR to precisely
181 quantify the abundance of the *LMNA, LMNC,* and *Progerin* transcripts in progeroid mouse tissues
182 and observed that *Progerin* makes up a minor proportion of the transcripts produced from the
183 *LMNA* locus (Fig. 1F), yet these same tissues produce high levels of Progerin protein (Fig. 1C-
184 D). The proportional abundance of *Progerin* transcript and Progerin protein are thus very poorly
185 correlated (Fig. 1G). Taken together, these data indicate that Lamin A, Lamin C, and Progerin
186 protein levels are post-transcriptionally modulated in human and mouse tissues. Similarly poor
187 correlations between transcript and protein levels have been observed for extremely long-lived
188 proteins, such as components of the nuclear pore complex(*23*), leading us to speculate that Lamin
189 A/C and/or Progerin are also long-lived proteins.
190
191 ***Lamin A/C/Progerin are long-lived proteins in the cardiovascular system***
192
193 To test the hypothesis that the A-type Lamins have long lifetimes, we sought to determine
194 the turnover rates of these proteins within the tissues of healthy and progeroid mice. Proteome-
195 wide quantification of protein stability can be achieved *in vivo* by supplying mice with chow
196 containing the stable, non-toxic isotope ^{15}N, then tracking the rate of incorporation of ^{15}N-labeled
197 amino acids into the proteome over time by mass spectrometry(*14*, *24*). We recently used ^{15}N
198 metabolic labeling to profile trends in protein turnover across healthy mouse tissues(*14*), and here
199 applied the same 6-timepoint, 32-day labeling timecourse approach to age-matched $LMNA^{G609G/+}$
200 mice. These mice exhibit weight loss, bone abnormalities, atherosclerosis, and cardiac
201 dysfunction before succumbing to the disease between 9 and 12 months of age(*5*). We focused
202 our analyses on young adult mice at early stages of disease (9 to 12 weeks of age), and quantified
203 protein lifetimes in tissues that exhibit progeroid pathology (the aorta, heart, and white adipose

Figure 2.

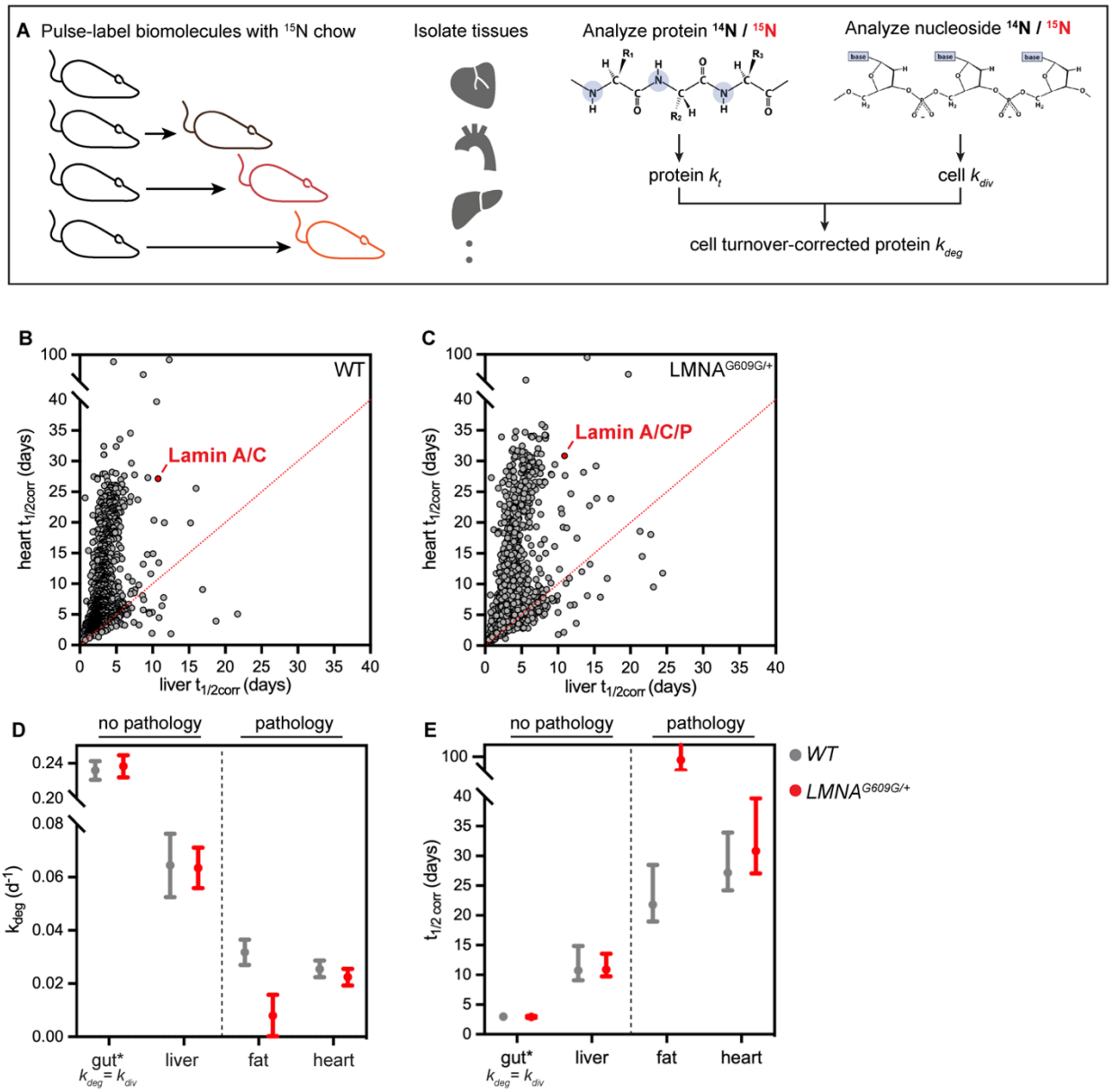

Figure 2. (A) Diagram of turnover and replication by ^{15}N isotope labeling (TRAIL) method for determining protein turnover (k_t) and cell turnover (k_{div}) by tracking ^{15}N incorporation into newly synthesized protein and genomic DNA, respectively. These two parameters are used to determine average bulk cell cycle-corrected protein degradation rates (k_{deg}). (B-C) Distribution of half-lives for proteins detected in both the liver and heart of healthy (B) and *LMNA*$^{G609G/+}$ (C) mice. The A-type Lamin proteins (red) are among a group of outliers with a dramatically longer lifetime in the heart than in the liver. (D-E) Cell cycle-corrected protein degradation rates (k_{deg}) (D) and half-lives ($t_{1/2corr}$) (E) for A-type Lamin proteins in tissues of healthy (gray) and *LMNA*$^{G609G/+}$ (red) mice. * denotes that A-type Lamin turnover is equivalent to cell turnover rate in the gut.

tissue) as well as tissues that are spared from disease (the intestine and liver). We defined protein turnover rates (k_t) and corresponding predicted half-life ($t_{1/2}$) values for 2744 proteins in the large intestine, 2098 proteins in the liver, 1881 proteins in the aorta, 1429 proteins in the white adipose tissue, and 1608 proteins in the heart (Fig. S4A-B; Table S1). Consistent with our previous analyses in healthy tissues, proteins generally turn over more rapidly in the progeroid intestine

210 (median $t_{1/2}$ 1.6 days) and liver (median $t_{1/2}$ 2.7 days) than in the progeroid aorta (median $t_{1/2}$ 3.8
211 days), heart (median $t_{1/2}$ 7.1 days) or fat (median $t_{1/2}$ 9.2 days).

212 While the goal of these experiments is to determine whether the A-type Lamins exhibit
213 variable lifetimes across tissues, a major confounding factor limits our ability to interpret
214 differences in protein lifetimes across tissues *in vivo*: the influence of cell turnover. That is, protein
215 turnover *in vivo* is shaped both by selective proteolytic degradation and non-selective dilution
216 during cell turnover. We recently developed a method, turnover and replication analysis by ^{15}N
217 isotope labeling (TRAIL) (Hasper et al 2022), to quantify both protein and cell lifetimes from the
218 same ^{15}N-labeled tissues to determine cell turnover-corrected protein degradation rates (Fig. 2A).
219 We applied this method to determine cell turnover rates (k_{div}) and doubling times within progeroid
220 intestine, liver, fat, and heart (Fig. S4C-D; Table S2). (Cell turnover was not determined for the
221 aorta due to limited sample.) Overall, cell doubling times were similar in progeroid and healthy
222 tissues with one exception: the white adipose tissue, where progeroid cells had a doubling time
223 of ~55 days while age-matched wild type cells had a doubling time of ~78 days. This observation
224 likely reflects increased proliferation and/or increased death of adipocytes, which are the most
225 abundant cell type found in fat depots. Notably, over-expression of Progerin blocks the terminal
226 differentiation of adipocyte precursors(*25*), and HGPS patients suffer from severe
227 lipodystrophy(*26*). We speculate that *LMNA*$^{G609G/+}$ mice are in the early stages of lipodystrophy at
228 9 weeks of age, as these animals are indistinguishable in weight compared to their littermates(*5*)
229 (Fig. S5), although their fat depots are moderately decreased in size.

230 By subtracting cell turnover rates (k_{div}) from protein turnover rates (k_t), we extrapolated cell
231 cycle-corrected protein degradation rates (k_{deg}) and predicted half-lives ($t_{1/2corr}$) for proteins in the
232 progeroid intestine, liver, heart, and fat. As we previously observed in wild type animals(*14*),
233 protein turnover rates vary widely across tissues even after cell cycle correction (Fig. 2B-C; Fig.
234 S4F; Table S1). We infer that the rate of cell division as well as environmental factors such as
235 local metabolism or the activity and selectivity of proteostasis networks shape protein lifetimes
236 across tissues(*14*).

237 We were able to determine the average turnover behavior of the Lamin A, Lamin C, and
238 Progerin proteins. We find that the A-type lamins have highly variable lifetimes across both
239 healthy and progeroid tissues. The distribution of half-lives for proteins detected in both the liver
240 and heart tissue of wild type (Fig. 2B) and progeroid (Fig. 2C) animals illustrates this point, as the
241 A-type lamins are among a small group of outlier proteins that have a dramatically longer lifetime
242 in the heart than in the liver. Overall, the lifetimes of the A-type lamins are longer in tissues that
243 exhibit progeroid pathology (the aorta, heart, and fat) compared to those that are spared from

244 pathology (the liver and intestine) in both wild type and progeroid animals (Table S1). After using
245 TRAIL to quantify cell turnover rates and determine corrected protein turnover rates, the
246 differences between A-type lamin turnover flux across these tissues were even more stark (Fig.
247 2B-C; cell turnover not determined for the aorta due to limited sample); indicating that these
248 proteins turn over dramatically more slowly in the fat and the heart. After cell cycle correction, the
249 predicted half-life for Lamin A/C in the healthy heart and fat is approximately 3 weeks. Further,
250 the average turnover rate of the closely related Lamin A, Lamin C, and Progerin proteins is slowed
251 to >1 month in the progeroid heart and fat compared to healthy tissues, raising the possibility that
252 the mutant Progerin protein turns over even more slowly than wild type Lamin A/C (Fig. 2E).
253
254 ***Biochemical influences on Lamin A/C and Progerin protein lifetime***

Figure 3.

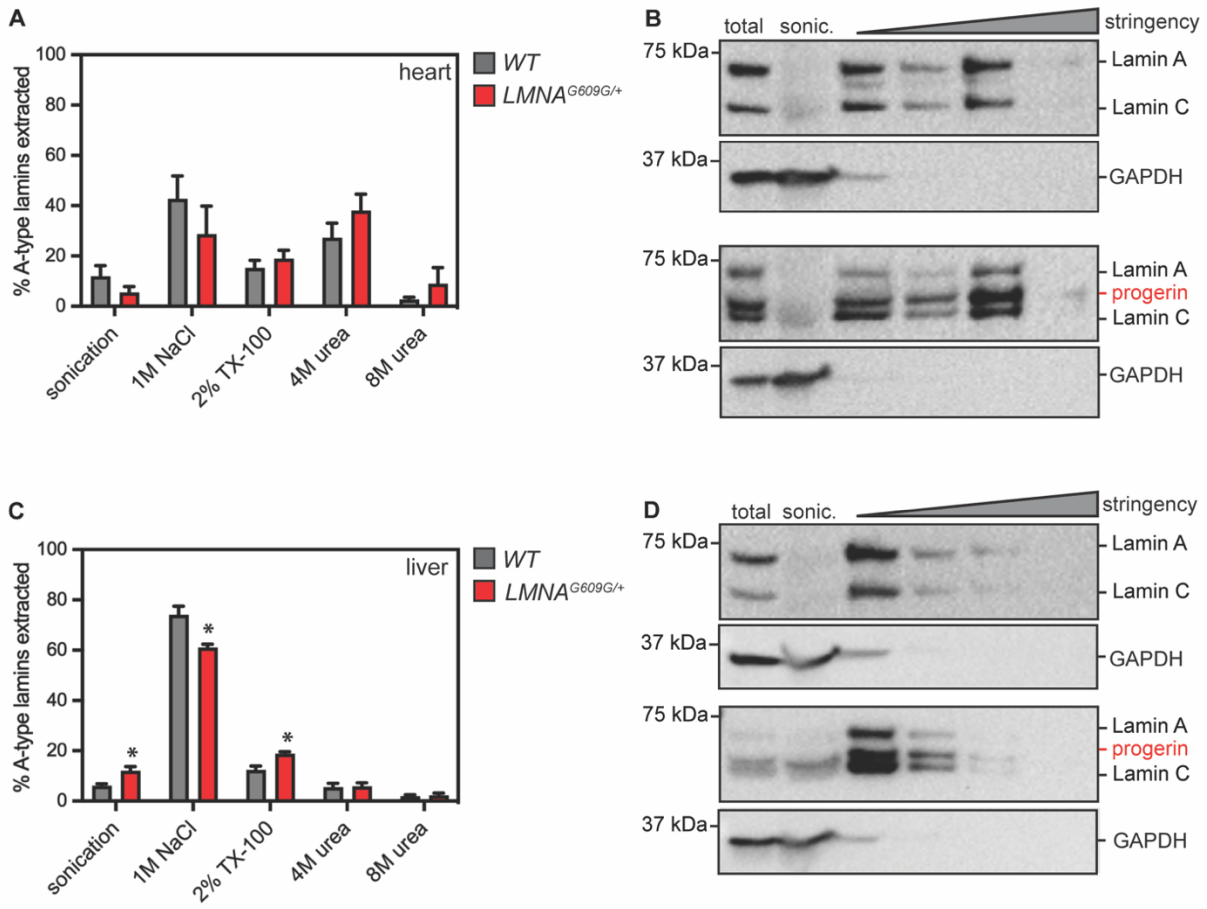

Figure 3. Serial extraction of LAmin A/C/Progerin proteins from heart (A-B) or liver (C-D) tissue of 4-month-old healthy and *LMNA*$^{G609G/+}$ mice. GAPDH indicates effective lysis and reelase of cytosol in each tissue. While Lamin A/C/Progerin are readily extractable with high salt in the liver (C-D) strong denaturants are required to completely extract these proteins
255 from the heart (A). * indicates significant differences in protein solubility between wild type and *LMNA*$^{G609G/+}$ liver tissue.

256 Why are the A-type Lamins readily turned over in the liver, but more slowly turned over in
257 the heart? The lamins form head-to-tail filaments that bundle laterally(*27*) and stiffen(*28*) or
258 undergo structural changes(*29*) in response to mechanical force. Because the heart is a
259 contractile tissue under high strain, we hypothesized that differences in the folding and/or
260 assembly state of the Lamin proteins in the heart might underlie the proteins' longer lifetime in
261 this tissue. To test this hypothesis, we subjected tissue homogenates to sequential extractions of
262 increasing stringency - using salt, detergent, and denaturants(*30*) – and compared the extent of
263 Lamin A/C/Progerin extraction after each step. These analyses indicated that the A-type lamins
264 are poorly extractable in heart tissue, where complete extraction was possible only in strongly
265 denaturing conditions (4M urea) (Fig. 3A-B). In the liver, in contrast, the A-type lamins were
266 efficiently extracted by treatment with high salt (Fig. 3C-D). These observations strongly imply
267 physicochemical differences in the assembly state of the Lamin polymers that correlate with the
268 differences in protein turnover rate between these tissues.

269 ***Progerin exhibits impaired turnover and accumulates in the cardiovascular system***

270

271 Progerin retains a hydrophobic lipid modification that is only transiently present on wild-
272 type Lamin A(*31*), raising the possibility that this disease variant could be more aggregation-prone
273 and/or more recalcitrant to turnover than the normal protein. Lamin A is synthesized as a pre-
274 protein that matures through a series of post-translational modifications. These include a lipid
275 modification (farnesylation) followed by proteolytic cleavages that remove the lipid-modified C-
276 terminus to generate mature Lamin A(*32*). The HGPS mutation deletes a key protease cleavage
277 site(*31*), generating the constitutively farnesylated Progerin protein. We could not determine
278 whether these closely related isoforms exhibit distinct turnover rates by shotgun proteomics (Fig.
279 2), as the small subset of peptides that distinguish Lamin A, Lamin C, or Progerin from each other
280 were not detected.

281 To determine whether the HGPS mutation extends protein lifetime, we
282 immunoprecipitated the A-type lamins from metabolically labeled progeroid heart, aorta, and liver
283 and performed parallel reaction monitoring mass spectrometry (PRM-MS)(*33*) to quantify
284 peptides unique to Lamin A *versus* Progerin (Fig. 4A-B; Table S3). We did not monitor Lamin-C-
285 only peptides, as Lamin C is distinguishable from Lamin A only at its C-terminal 6 amino acids,
286 and this region does not generate any quantifiable and unique tryptic peptides. For maximum
287 sensitivity, we focused our analyses on the labeling timepoint that was closest to the predicted
288 half-life of the A-type lamins in each tissue: 32 days for the heart, 16 days for the aorta, and 8

289 days for the liver. By quantifying the $^{15}N/^{14}N$ isotope abundance ratio for individual peptides unique
290 to each protein isoform, we could compare the relative extent of turnover. These analyses
291 revealed that Progerin turns over significantly more slowly than wild type Lamin A in the heart
292 (Fig. 4C-E) and aorta (Fig. 4F-H) but not in the liver (Fig. 4I-K). Comparing these isoform-resolved
293 data to our bulk A-type lamin turnover data (Table S3) leads us to estimate that Progerin's lifetime
294 within the cardiovascular system is on the order of months. Altogether, these protein turnover

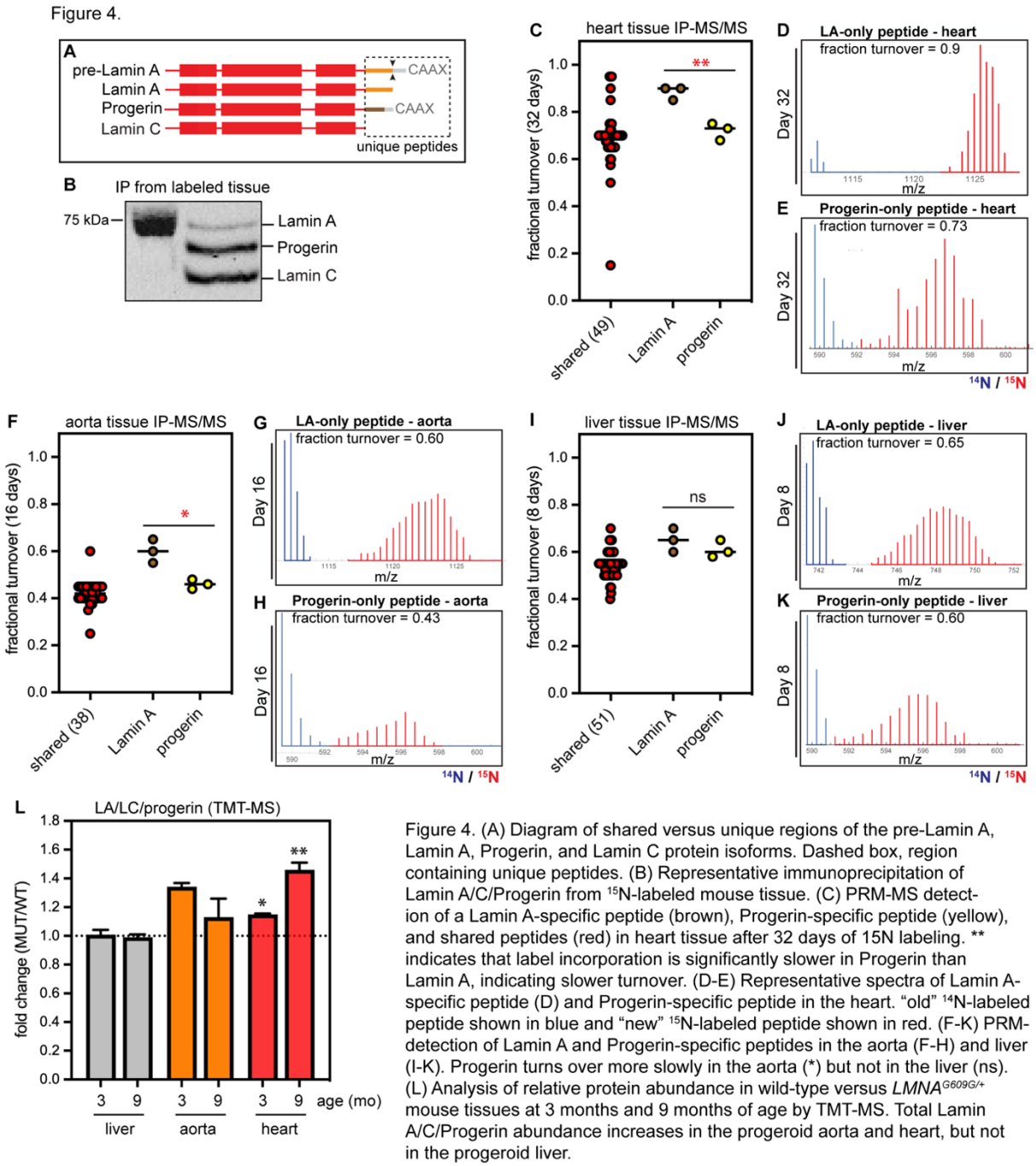

Figure 4. (A) Diagram of shared versus unique regions of the pre-Lamin A, Lamin A, Progerin, and Lamin C protein isoforms. Dashed box, region containing unique peptides. (B) Representative immunoprecipitation of Lamin A/C/Progerin from ^{15}N-labeled mouse tissue. (C) PRM-MS detection of a Lamin A-specific peptide (brown), Progerin-specific peptide (yellow), and shared peptides (red) in heart tissue after 32 days of 15N labeling. ** indicates that label incorporation is significantly slower in Progerin than Lamin A, indicating slower turnover. (D-E) Representative spectra of Lamin A-specific peptide (D) and Progerin-specific peptide in the heart. "old" ^{14}N-labeled peptide shown in blue and "new" ^{15}N-labeled peptide shown in red. (F-K) PRM-detection of Lamin A and Progerin-specific peptides in the aorta (F-H) and liver (I-K). Progerin turns over more slowly in the aorta (*) but not in the liver (ns). (L) Analysis of relative protein abundance in wild-type versus *LMNA*$^{G609G/+}$ mouse tissues at 3 months and 9 months of age by TMT-MS. Total Lamin A/C/Progerin abundance increases in the progeroid aorta and heart, but not in the progeroid liver.

295

296 analyses indicate that both tissue context and disease mutations modulate the lifetime of the A-
297 type lamin proteins.

298 If Progerin turnover is impaired compared to wild type Lamin A, one might predict that
299 Progerin would accumulate over time. We used tandem mass tagging (TMT) and proteomics(*34*)
300 to quantify relative protein abundance in healthy *versus* progeroid tissues from young adult mice
301 (3 months old) and from animals nearing the end of the HGPS mouse lifespan (9 months old).
302 These data indicated that the total dose of A-type lamin proteins is significantly increased in the
303 progeroid heart, but not the liver; while the dose of these proteins trends upward in the diseased
304 aorta, this trend is not significant due to variability across samples (Fig. 4L). Because this analysis
305 cannot distinguish Progerin from Lamin A, these data could indicate either that Progerin
306 accumulates over time, or that Progerin also interferes with the turnover of wild-type Lamin A,
307 leading to accumulation of all A-type lamin isoforms in diseased tissue.

Figure 5.

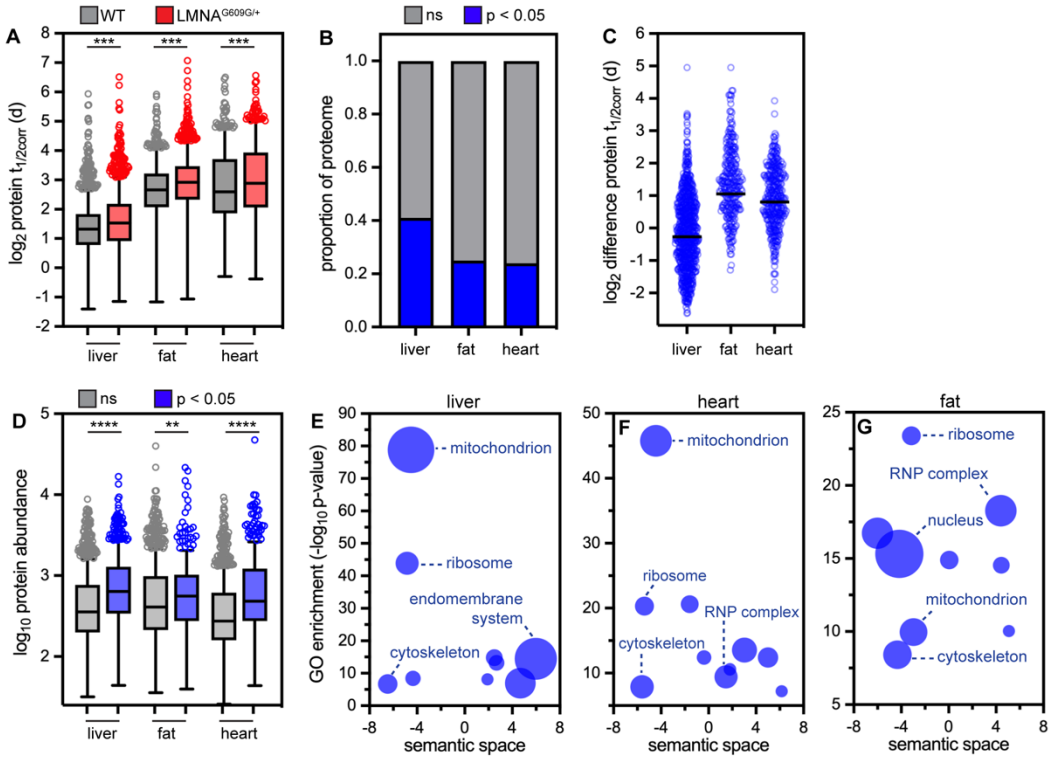

Figure 5. (A) Predicted protein half-lives determined for proteins in liver, fat, and heart muscle of 3-month-old healthy and *LMNA*$^{G609G/+}$ mice. *** indicates a significant decrease in protein turnover flux in progeroid tissues. Data from wild type animals reproduced from Hasper et al., *Mol Syst Biol* 2023. (B) Proportion of proteins in each tissue with significantly different turnover rates in progeroid animals versus wild type animals (t-test). (C) Difference in protein lifetime (MUT-WT) for proteins with significantly different lifetimes in progeroid animals versus wild type animals. Liver median difference = + 0.8 days (n = 841); fat median difference +2.1 days (n = 349); heart median difference +1.75 days (n = 373). (D) Comparison of protein abundance between proteins with significantly altered lifetime in progeroid tissue (blue) versus proteins with unchanged lifetime in progeroid tissue (gray). **** indicates that proteins with impaired turnover in progeroid tissue are more abundant than proteins with unchanged turnover in progeroid tissue (Mann-Whitney test). (E-G) Subsets of Gene Ontology (GO) terms (cellular component) over-represented in proteins with significantly slower turnover in progeroid tissues compared to healthy tissues. Redundant GO terms were removed and non-redundant GO terms organized based on semantic similarity with REViGO. Bubble size corresponds to number of proteins associated with the GO term, ranging in size from 12 to 175 (E), 14 to 95 (F), and 10 to 157 (G).

308

309 ***Progerin expression impairs global proteostasis***

310 Our data indicate that the Progerin disease variant accumulates selectively within the
311 cardiovascular system over time. We hypothesized that as Progerin accumulates within diseased
312 tissue, it could sequester other proteins and interfere with their turnover. Consistent with this
313 hypothesis, we observed global changes in protein stability in progeroid tissues (Fig. 5A). At an
314 individual protein level, 24-40% of quantified proteins have significantly extended lifetimes in
315 progeroid tissues compared to healthy tissues (Fig. 5B). The magnitude of this effect is most
316 pronounced in the heart and adipose tissue, where this subset of proteins experience a median
317 lifetime extension of approximately 2 days compared to age-matched wild-type animals (Fig. 5C).
318 These proteins are constituents of various protein structures including mitochondria, ribosomes,
319 the nucleus, and the cytoskeleton (Fig. 5E-G). As these proteins are components of such diverse
320 cellular structures, we hypothesized that shared physicochemical features, not protein
321 localization, might underlie their sensitivity to Progerin expression. Indeed, we found that
322 Progerin-sensitive proteins are much more abundant than Progerin-insensitive proteins (Fig. 5D).
323 Altogether, the ability of Progerin to impair the turnover of abundant proteins associated with a
324 broad range of cellular structures is consistent with an aggregation-based mechanism of toxicity,
325 as highly abundant proteins are more vulnerable to aggregation(*35*, *36*)

326

327 ***Human disease alleles are over-represented in the long-lived proteome***

328

329 Our data suggest that protein lifetime modulates the effects of disease-causative
330 mutations to cause tissue-specific disease. To explore the relationship between protein lifetime
331 and human disease more systematically, we evaluated the distributions of proteins linked to
332 human disease across our recently acquired datasets of protein turnover rates in healthy mouse
333 heart, liver, and adipose tissues(*37*). We quantified the turnover rates of ~1600 to ~2100 proteins
334 per tissue, and found that mutations in ~600 to ~800 of those proteins are linked to human disease
335 in the OMIM database. Evaluating the distributions of these disease-linked proteins across
336 turnover rate deciles revealed that proteins linked to human disease are significantly over-
337 represented in the most long-lived proteins in each tissue – with the most dramatic over-
338 representation apparent in the heart (Fig. 5A, Table I, Table S4). Selected disease-linked proteins
339 found in the 1st decile of turnover rates in heart, liver, or fat are shown in Table I (see Table S4
340 for complete list). In addition to *LMNA,* mutations to *CAV3, ACTA1, ACTC1, DYSF,* and *DSG2*
341 are linked to cardiomyopathies and encode proteins that are long-lived in the heart. Some of these
342 proteins, such as ACTA1 and ACTC1, are selectively expressed in cardiac muscle, which

Figure 5.

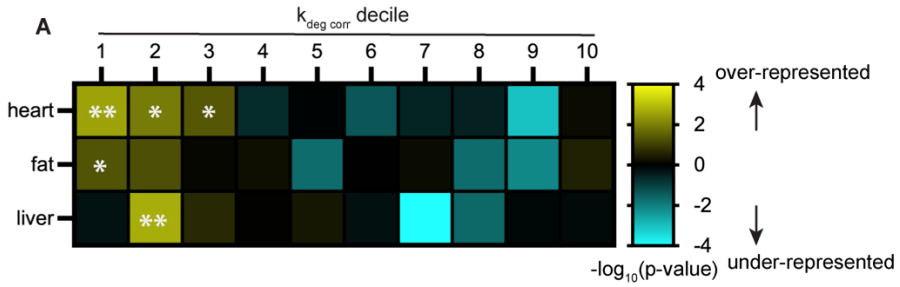

Table I. Long-lived proteins and human disease

Tissue	Name	Uniprot ID	k_{deg} (d^{-1})	$t_{1/2corr}$ (d)	Disease	OMIM
heart	CAV3	P51637	0.010 ± 0.003	68.9	Tateyama type distal myopathy	614321
					Familial hypertrophic cardiomyopathy	192600
					Long QT syndrome	611818
	ACTA1	P68134	0.016 ± 0.005	42.2	Nemaline myopathy	161800
	DYSF	Q9ESD7	0.024 ± 0.003	29.4	Limb-girdle muscular dystrophy	253601
					Miyoshi muscular dystrophy	254130
	LMNA	P48678	0.026 ± 0.003	26.7	Dilated cardiomyopathy	115200
					Emery-Dreifuss muscular dystrophy	616516
					Hutchinson-Gilford progeria syndrome	176670
					Congenital muscular dystrophy	613205
	DSG2	O55111	0.029 ± 0.005	24.0	Arrhythmogenic right ventricular dysplasia	610193
	ACTC1	P68033	0.031 ± 0.003	22.2	Left ventricular noncompaction	613424
					Hypertrophic cardiomyopathy	612098
					Atrial septal defect	612794
					Dilated cardiomyopathy, dilated	613424
fat	LMNA	P48678	0.032 ± 0.005	21.8	Familial partial lipodystrophy	151660
liver	KRT18	P05784	0.059 ± 0.012	11.7	Cryptogenic cirrhosis	215600
	AGL	F8VPN4	0.064 ± 0.008	10.9	Glycogen storage disease IIIa/IIIb	232400

Figure 5. (A) Analysis of distribution of human disease alleles (OMIM) across deciles of protein turnover rates in healthy mouse tissues. Map color indicates significance of over-representation (yellow) or under-representation (blue) of disease alleles in each decile. ** indicates that human disease alleles are significantly over-represented in the 1st, 2nd, and 3rd deciles of k_{deg} rate (most long-lived) in the heart; in the 1st decile in the fat; and in the 2nd decile in the liver (Fisher's exact test). Table II shows protein turnover rate data for selected long-lived proteins linked to human disease. Data re-analyzed from Hasper et al., BioRXiV 2022. See Table S4.

provides an obvious explanation for the tissue-specific consequences of mutations. However, similarly to Lamin A/C, the DYSF, DSG2, and CAV3 proteins are expressed in several tissues but are only long-lived in the heart (Fig. S6C-E), while the proteins KRT18 and AGL are broadly expressed but are only long-lived in the liver (Fig. S6F-G), where their mutations cause disease. These analyses overall reveal an unexpected enrichment of human disease alleles in extremely long-lived proteins and suggest that protein lifetime may influence disease etiology not just in laminopathies but also in other monogenetic human diseases.

352 **Discussion**

353

354 In this study, we applied quantitative proteomic approaches to explore the origins of tissue
355 specificity in laminopathy syndromes, which are caused by mutations to the abundant and broadly
356 expressed Lamin A/C protein. We determined that the Lamin A/C proteins have significantly
357 longer lifetimes within the cardiovascular system and fat, which are disrupted in laminopathies,
358 while these proteins have shorter lifetimes in disease-spared tissues such as the liver and
359 intestine. We demonstrated that the A-type Lamins are more densely bundled and less
360 extractable in the heart than in the liver. Since substrate unfolding is the major rate-limiting step
361 in protein degradation(*38*), more densely bundled Lamin polymers may be more recalcitrant to
362 protein turnover than the same proteins in a less densely bundled state. In the future, it will be
363 important to explore how Lamin assembly state modulates the functions of the nuclear lamina.

Figure 7.

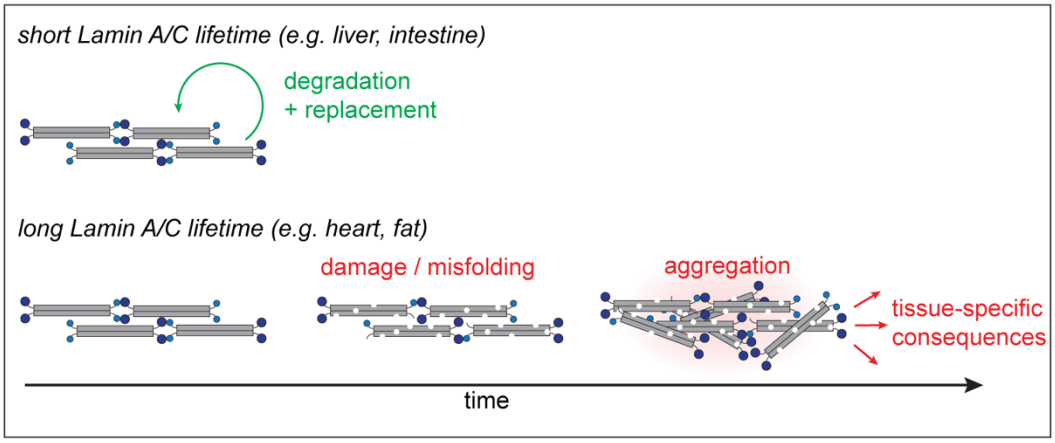

Figure 7. Working model of interplay between protein turnover rate and time- and mutation-dependent accumulation of dysfunction in progeroid tissues.

364 Our findings suggest that HGPS and other laminopathies may arise as a consequence of
365 disrupted proteostasis. In some tissues (such as the liver), the A-type Lamins may be maintained
366 in a folded and functional state by consistent degradation and replacement (Fig. 7). In tissues
367 where the Lamins are long-lived (such as the heart), in contrast, protein synthesis and
368 degradation happen rarely. In this context, these long-lived proteins may undergo molecular
369 "aging" – meaning that they may accumulate damage, misfold, and perhaps irreversibly aggregate
370 in a time-dependent manner. Laminopathy-linked mutations may increase the propensity for
371 misfolding and/or irreversible aggregation over time, leading to the tissue-specific and time-
372 dependent accumulation of dysfunction. We found that the turnover of the HGPS-causative
373 Progerin mutant is selectively impaired within the cardiovascular system, leading to its
374 accumulation over time (Fig. 4). By analogy to neurodegenerative diseases caused by protein

375 aggregation(*39*), Progerin aggregates could exert broad and pleiotropic influence on protein
376 quality control by inducing co-aggregation of other proteins and/or by acting as a sink for the
377 proteostasis machinery. Indeed, we observe impaired turnover of hundreds of abundant proteins
378 in progeroid tissues (Fig. 5). These proteins include constituents of mitochondria, ribosomes, the
379 nucleus and the cytoskeleton, and dysfunction related to each of these cellular structures has
380 been reported in HGPS(*13*, *40–42*). Decreased proteasome activity has been reported in
381 fibroblasts derived from HGPS patients(*13*, *43*), leading us to speculate that decreased flux
382 through the proteasome could contribute to extension of protein lifetimes that we observe.
383 All gene therapies rely on a key assumption: that targeting a gene or transcript will lead to
384 the desired changes to the encoded protein. We have demonstrated that Progerin is a long-lived
385 and toxic mutant protein. Because long-lived proteins are rarely synthesized and rarely degraded,
386 they are relatively insensitive to changes in their synthesis rate(*23*). This explains why gene
387 therapies have significant latency and limited potency in decreasing Progerin protein levels in the
388 cardiovascular system(*6*). Interestingly, combination treatment with a farnesyltransferase
389 inhibitor, which interferes with the biosynthesis of Progerin at the protein level, results in more
390 robust clearance of the mutant protein(*6*). Further exploration of orthogonal approaches for
391 interfering with Progerin protein production or accelerating protein degradation may identify new
392 therapies for this devastating disease.
393 By evaluating the relationship between human disease alleles and protein lifetime, we
394 discovered that disease-linked proteins are generally over-represented in the long-lived
395 proteome. As we have demonstrated in the context of HGPS, long protein lifetime may exert an
396 important influence on protein function and present a major barrier to treatment in numerous
397 human disease states.
398
399 **Materials and Methods**
400
401 **Mouse model**
402 All animal experiments were performed in compliance with relevant ethical regulations and with
403 approval by the Institutional Animal Care and Use Committee at UCSF (IACUC protocol number
404 AN178187, PI: A.B.).
405
406 **Protein extraction from mouse tissues for Western blotting**
407 Approximately 30 milligrams of frozen tissue was excised on dry ice with a clean razorblade and
408 placed in a fresh tube. 100 uL of urea lysis buffer (ULB: 8M urea, 75 mM NaCl, 50 mM HEPES

409 pH 7.9, protease and phosphatase inhibitors) was added to the tube, and the tissue was then
410 minced on ice with scissors. ULB was added to a final volume of 600 uL, and the sample was
411 transferred to a Dounce homogenizer. The sample was homogenized for ~40 strokes with the
412 tight pestle, then transferred to a clean microcentrifuge tube. The sample was then probe
413 sonicated at 4C (10% amplitude, 10 seconds, 2 cycles) before being centrifuged (21,000 x g, 11
414 minutes, 4C). The supernatant was transferred to a clean tube. Protein concentration was
415 quantified by microBSA assay (Pierce). Lysates were mixed with SDS-PAGE sample buffer,
416 heated to 95°C for 5 minutes, and cooled. 20 micrograms of protein were loaded per well for
417 Western blot analysis and proteins were detected with an HRP-conjugated mouse monoclonal
418 antibody that recognizes an N-terminal epitope shared in Lamin A, Lamin C, and Progerin (Santa
419 Cruz sc-376248). Blots were visualized on a Chemi-Doc (BioRad) and proportional abundance of
420 each protein isoform was determined by densitometry.
421
422 **Serial extractions of protein from mouse tissues**
423 Relative solubility of the Lamin proteins was assayed using a serial extraction protocol adapted
424 from (*30*). Approximately 20 milligrams of frozen tissue was excised on dry ice with a clean
425 razorblade and placed in a fresh tube. Buffer 1 (10 mM HEPES pH 7.4, 2 mM MgCl2, 25 mM KCl,
426 250 mM sucrose, 1 mM DTT, protease and phosphatase inhibitors; 300 uL) was added to the
427 tube, and tissue was minced on ice. The sample was transferred to a Dounce homogenizer and
428 homogenized for ~40 strokes with the tight pestle, then transferred to a clean microcentrifuge
429 tube. The sample was probe sonicated at 4C (10% amplitude, 5 seconds, 2 cycles); a 50 uL
430 aliquot (whole tissue lysate) was retained. The remaining sample was then centrifuged (20,000 x
431 g, 5 minutes, 4C). The supernatant (S1) was retained. The pellet was resuspended in Buffer 2
432 (20 mM HEPES pH 7.4, 1 M NaCl, protease and phosphatase inhibitors; 250 uL) and incubated
433 20 minutes at RT with end-over-end rotation. The sample was then centrifuged (20,000 x g, 5
434 minutes, RT) and the supernatant (S2) was retained. The pellet was resuspended in Buffer 3 (20
435 mM HEPES pH 7.4, 1 M NaCl, 2% Triton-X-100, protease and phosphatase inhibitors; 250 uL)
436 and incubation and centrifugation were repeated. The supernatant (S3) was retained and the
437 pellet was resuspended in Buffer 4 (20 mM HEPES pH 7.4, 1M NaCl, 4M urea, protease and
438 phosphatase inhibitors; 250 uL) and incubation and centrifugation were repeated. Finally, the
439 supernatant (S4) was retained and the pellet was resuspended in Buffer 5 (20 mM HEPES pH
440 7.4, 1 M NaCl, 8M urea, protease and phosphatase inhibitors; 250 uL) and incubation and
441 centrifugation were repeated. The final supernatant (S5) was retained. An aliquot of the tissue
442 lysate and equal proportions of each supernatant were loaded on SDS-PAGE gels and processed

443 for Western blotting with an HRP-conjugated mouse monoclonal antibody that recognizes an N-
444 terminal epitope shared in Lamin A, Lamin C, and Progerin (Santa Cruz sc-376248).
445
446 **RNA extraction from mouse tissues**
447 Approximately 30 milligrams of frozen tissue was excised on dry ice with a clean razorblade and
448 placed in a fresh microcentrifuge tube. 100 uL of TRIzol was added, and tissue was minced with
449 scissors on ice. Additional TRIzol was added to a final volume of 500 uL and the sample was
450 transferred to a Dounce homogenizer. The sample was homogenized for ~40 strokes with the
451 tight pestle, then transferred to a clean microcentrifuge tube. The sample was incubated for 5
452 minutes at RT before chloroform (100 uL) was added. The sample was mixed by inversion and
453 incubated for 3 minutes, then centrifuged (12,000 x g, 15 minutes, 4C). The aqueous RNA-
454 containing supernatant was carefully removed and pipetted into a fresh tube. 1 uL of GlycoBlue
455 and 250 uL isopropanol were added to the supernatant, incubated for 10 minutes at RT, then
456 centrifuged (12,000 x g, 10 minutes, 4C). The supernatant was removed from the blue RNA-
457 glycogen pellet, then the pellet was resuspended in 500 uL 75% ethanol and centrifuged (7500 x
458 g, 5 minutes, 4C). The supernatant was removed and the pellet was allowed to air dry for 5-10
459 minutes. The pellet was resuspended in 50 uL nuclease-free water (Ambion) and RNA
460 concentration was determined by NanoDrop.
461
462 **Transcript quantification with digital droplet PCR**
463 For each sample, 1 ug of RNA was diluted into 15 uL reverse transcription reactions using the
464 iScript RT kit (Bio-Rad) and reactions were carried out following the manufacturer's instructions.
465 Each cDNA reaction was diluted to 10 ng/uL (RNA equivalents). For each sample, 20 ng (RNA
466 equivalents) was combined with 10 uL of 2x ddPCR Supermix for Probes (no UTP; Bio-Rad), 1
467 uL of a 20x FAM primer/probe set, 1 uL of a HEX primer/probe set, and nuclease free water to a
468 final volume of 20 uL. *Lmna* primers and probe sequences are listed below and are adapted
469 from(*6*). *mTfrc* primers and probe sequence was from Bio-Rad (PrimerPCR ddPCR Expression
470 Probe Assay for Tfrc Mouse (HEX)). Reaction droplets were generated on a Droplet Maker (Bio-
471 Rad); ddPCR reactions were run on a C1000 Thermocycler (Bio-Rad); and reactions were
472 analyzed on a QX100 ddPCR reader (Bio-Rad) according to the manufacturer's instructions.
473 ddPCR allows the absolute quantification of transcript abundance based on the ratio of positive
474 to negative droplets and is unaffected by primer-specific variables such as reaction efficiency(*44*).
475 We used absolute ddPCR quantification to determine the abundance of the *Lmna*, *Lmnc,* and
476 *Progerin* transcripts (copies per droplet). *mTfrc* reactions were run in the HEX channel of each

477 ddPCR reaction as a positive control, but were not used to normalize *Lmna* transcript
478 measurements. Transcript abundance was expressed as a proportion for each transcript. For
479 example, for *Lmna*:
480
481 proportional abundance *Lmna = [Lmna]/([Lmna] + [Lmnc] + [Progerin])*
482
483 ddPCR probe and primersets for mouse *Lmna, Lmnc,* and *Progerin* were as previously
484 described(*6*) and as listed in the following table.

Target	Primer (F)	Primer (R)	Probe
Lamin A (FAM)	ACCGCTCTCATCAACTCCAC	GCGGCGGCTGCCACTCAC	GGTTGAGGACAATGAGGATG
Progerin (FAM)	AGAAGAGCTCCTCCATCACC	ACATGATGCTGCAGTTCTGG	TGGAGCGGGAGCCCAGAGCTC
Lamin C (FAM)	ATCCATCTCCTCTGGCTCTT	ACATGATGCTGCAGTTCTGG	TCCAGTCCCCGGAGCCAG/AGCT

485
486 **Metabolic labeling of mice and tissue isolation**
487 As recently described(*14*), we performed a 6-timepoint, 32-day ^{15}N labeling timecourse (0, 2, 4,
488 8, 16, and 32 days of labeling) with a total of 3 animals of both sexes per labeled timepoint, and
489 2 animals for the day 0 (unlabeled) timepoint. Timecourses were performed in *LMNA*$^{G609G/+}$
490 C57Bl/6 mice at approximately 9 weeks of age. ^{14}N and ^{15}N mouse chow was obtained from
491 Silantes. Animals were first habituated to the chow formulation by feeding ^{14}N (normisotopic) food
492 for 1 week; animals were then transitioned to ^{15}N chow throughout the labeling period (roughly 3
493 grams / animal / day). Animals were sacrificed by CO_2 inhalation followed by cervical dislocation,
494 followed by tissue dissection and flash freezing by submersion in liquid nitrogen.
495
496 **Protein extraction and sample preparation for LC-MS/MS**
497 *Protein extraction:* Approximately 30 milligrams of frozen tissue was excised on dry ice with a
498 clean razorblade and placed in a fresh tube. 100 uL of protein extraction buffer (PEB: 5% SDS,
499 100 mM TEAB, protease and phosphatase inhibitors, pH ~7) was added to the tube. The tissue
500 was minced on ice; PEB was added to bring the final volume to 600 uL, then the sample was
501 transferred to a Dounce homogenizer. The sample was homogenized for ~40 strokes with the
502 tight pestle, then transferred to a clean microcentrifuge tube. The sample was then probe
503 sonicated at 4C (10% amplitude, 10 seconds, 2 cycles) before being centrifuged (21,000 x g, 11
504 minutes, 4C). The supernatant was transferred to a clean tube, and aliquots were separated for
505 proteomics and protein quantification by microBSA assay (Pierce).

506 *Trypsinization:* Samples were diluted to 1 mg/mL in 5% SDS, 100 mM TEAB, and 25 µg of protein
507 from each sample was reduced with dithiothreitol to 2 mM, followed by incubation at 55°C for 60
508 minutes. Iodoacetamide was added to 10 mM and incubated in the dark at room temperature for
509 30 minutes to alkylate proteins. Phosphoric acid was added to 1.2%, followed by six volumes of
510 90% methanol, 100 mM TEAB. The resulting solution was added to S-Trap micros (Protifi), and
511 centrifuged at 4,000 x g for 1 minute. The S-Traps containing trapped protein were washed twice
512 by centrifuging through 90% methanol, 100 mM TEAB. 1 µg of trypsin was brought up in 20 µL of
513 100 mM TEAB and added to the S-Trap, followed by an additional 20 µL of TEAB to ensure the
514 sample did not dry out. The cap to the S-Trap was loosely screwed on but not tightened to ensure
515 the solution was not pushed out of the S-Trap during digestion. Samples were placed in a humidity
516 chamber at 37°C overnight. The next morning, the S-Trap was centrifuged at 4,000 x g for 1
517 minute to collect the digested peptides. Sequential additions of 0.1% TFA in acetonitrile and 0.1%
518 TFA in 50% acetonitrile were added to the S-trap, centrifuged, and pooled. Samples were frozen
519 and dried down in a Speed Vac (Labconco) prior to TMTpro labeling.

520 *TMT labeling*: Samples were reconstituted in TEAB to 1 mg/mL, then labeled with TMTpro 16plex
521 reagents (Thermo Fisher) following the manufacturers protocol. Briefly, TMTpro tags were
522 removed from the -20°C freezer and allowed to come to room temperature, after which acetonitrile
523 was added. Individual TMT tags were added to respective samples and incubated at room
524 temperature for 1 hour. 5% hydroxylamine was added to quench the reaction, after which the
525 samples for each experiment were combined into a single tube. Since we performed abundance
526 quantitation on unlabeled peptides, 0 day samples were added to four of the unused channels,
527 increasing the signal for the unlabeled peptides. TMTpro tagged samples were frozen, dried down
528 in the Speed Vac, and then desalted using homemade C18 spin columns to remove excess tag
529 prior to high pH fractionation.

530 *High pH Fractionation:* Homemade C18 spin columns were activated with two 50 µL washes of
531 acetonitrile via centrifugation, followed by equilibration with two 50 µL washes of 0.1% TFA.
532 Desalted, TMTpro tagged peptides were brought up in 50 µL of 0.1% TFA and added to the spin
533 column. After centrifugation, the column was washed once with water, then once with 10 mM
534 ammonium hydroxide. Fractions were eluted off the column with centrifugation by stepwise
535 addition of 10 mM ammonium hydroxide with the following concentrations of acetonitrile: 2%,
536 3.5%, 5%, 6.5%, 8%, 9.5%, 11%, 12.5%, 14%, 15.5%, 17%, 18.5%, 20%, 21.5%, 27%, and 50%.
537 The sixteen fractions were concatenated down to 8 by combining fractions 1 and 9, 2 and 10, 3

538 and 11, etc. Fractionated samples were frozen, dried down in the Speed Vac, and brought up in
539 0.1% TFA prior to mass spectrometry analysis.

540 **LC-MS/MS Analysis**

541 *Data collection:* Peptides from each fraction were injected onto a homemade 30 cm C18 column
542 with 1.8 um beads (Sepax), with an Easy nLC-1200 HPLC (Thermo Fisher), connected to a Fusion
543 Lumos Tribrid mass spectrometer (Thermo Fisher). Solvent A was 0.1% formic acid in water,
544 while solvent B was 0.1% formic acid in 80% acetonitrile. Ions were introduced to the mass
545 spectrometer using a Nanospray Flex source operating at 2 kV. The gradient began at 3% B and
546 held for 2 minutes, increased to 10% B over 7 minutes, increased to 38% B over 94 minutes, then
547 ramped up to 90% B in 5 minutes and was held for 3 minutes, before returning to starting
548 conditions in 2 minutes and re-equilibrating for 7 minutes, for a total run time of 120 minutes. The
549 Fusion Lumos was operated in data-dependent mode, employing the MultiNotch Synchronized
550 Precursor Selection MS3 method to increase quantitative accuracy(*45*). The cycle time was set
551 to 3 seconds. Monoisotopic Precursor Selection (MIPS) was set to Peptide. The full scan was
552 done over a range of 400-1500 m/z, with a resolution of 120,000 at m/z of 200, an AGC target of
553 4e5, and a maximum injection time of 50 ms. Peptides with a charge state between 2-5 were
554 picked for fragmentation. Precursor ions were fragmented by collision-induced dissociation (CID)
555 using a collision energy of 35% and an isolation width of 1.0 m/z. MS2 scans were collected in
556 the ion trap with an AGC target of 1e4 and a maximum injection time of 35 ms. MS3 scans were
557 performed by fragmenting the 10 most intense fragment ions between 400-2000 m/z, excluding
558 ions that were 40 m/z less and 10 m/z greater than the precursor peptide, using higher energy
559 collisional dissociation (HCD). MS3 ions were detected in the Orbitrap with a resolution of 50,000
560 at m/z 200 over a scan range of 100-300 m/z. The isolation width was set to 2 Da, the collision
561 energy was 60%, the AGC was set to 1e5, and the maximum injection time was set to 100 ms.
562 Dynamic exclusion was set to 45 seconds.

563 *Data analysis*: Raw data was searched using the SEQUEST search engine within the Proteome
564 Discoverer software platform, version 2.4 (Thermo Fisher), using the Uniprot mouse database
565 (downloaded January 2020). Trypsin was selected as the enzyme allowing up to 2 missed
566 cleavages, with an MS1 mass tolerance of 10 ppm, and an MS2 mass tolerance of 0.6 Da.
567 Carbamidomethyl on cysteine, and TMTpro on lysine and peptide N-terminus were set as a fixed
568 modifications, while oxidation of methionine was set as a variable modification. Percolator was
569 used as the FDR calculator, filtering out peptides which had a q-value greater than 0.01. Reporter

570 ions were quantified using the Reporter Ions Quantifier node, with an integration tolerance of 20
571 ppm, and the integration method being set to “most confident centroid”. Protein abundances were
572 calculated by summing the signal to noise of the reporter ions from each identified peptide, while
573 excluding any peptides with an isolation interference of greater than 30%, or SPS matches less
574 than 65%.

575 *Kinetic model:* The kinetic model applied in this study has been previously described(*46*). Briefly,
576 we are assuming that protein synthesis is a zero order process, occurs at a constant fractional
577 rate, and that that the total protein concentration of each cell does not change during the
578 experimental time-course. The dilution of the protein pool due to cell division can be modeled as
579 a first order exponential process. Thus, the fractional turnover of unlabeled proteins during the
580 labeling time course can be regarded as a first order kinetic process that can be modelled based
581 on the following exponential equation:

582 $$\text{fraction unlabeled protein}(t) = e^{-k_t * t} \quad (1)$$

583 And:

584 $$k_t = k_{deg} + k_{div}$$

585 Where:

586 k_t is the clearance rate (observed rate of fractional labeling), k_{deg} is the rate of protein
587 degradation and k_{div} is the rate of cell division.

588 The determination of k_t values were conducted as previously described(*46*) using the decay of
589 the TMT reporter signals of unlabeled proteins. Protein-level TMT reporter abundances for
590 unlabeled proteins for each replicate experiment were first normalized by dividing by the intensity
591 of the t0 reporter and then the replicate experiments were aggregated in a single kinetic curve. In
592 fitting the exponential decay curves of the unlabeled protein signals, a constant fractional baseline
593 at infinite time was incorporated in the fitting equation. The equation used for fitting the curves
594 was therefore: $intensity = baseline + (1 - baseline) * e^{-k_t * time}$. The goodness of fit for least
595 squares fits were assessed by determining the R^2, P-value and t-statistic of the fits (see Supp
596 Table 1). For subsequent analyses, only protein k_t measurements that were obtained from all

597 three replicate experiments, incorporated data from 4 or more peptide spectral matches (PSMs),
598 and had t-statistic values greater than three were considered.

599 **Nucleic acid extraction and sample preparation for LC-MS/MS**

600 *Genomic DNA extraction:* Approximately 30 milligrams of frozen tissue was excised on dry ice
601 with a clean razorblade and placed in a fresh tube. 100 uL of TRIzol reagent (Invitrogen) was
602 added and the tissue was rapidly minced on ice. An additional 400 uL of TRIzol was added, and
603 the sample was then transferred to a Dounce homogenizer. The tissue was subjected to ~40
604 strokes with the tight pestle until smooth, then transferred back to the original tube. The sample
605 was incubated for at least 5 minutes before the addition of 100 uL chloroform followed by mixing
606 and a further 3 minutes of incubation. The sample was then centrifuged (12,000 x g, 15 minutes,
607 4C) and the upper RNA-containing aqueous layer was discarded. 150 uL of absolute ethanol was
608 added to the remaining sample, then inverted several times to mix. After 3 minutes of incubation
609 at room temperature, the sample was centrifuged (2,000 x g, 5 minutes, 4C). The protein-
610 containing supernatant was removed, then the DNA-containing pellet was resuspended in 500 uL
611 of absolute ethanol and incubated for 30 minutes. The sample was then centrifuged (2,000 x g, 5
612 minutes, 4C), and the supernatant discarded. Sequential washes were then repeated with 95%,
613 85%, and 75% ethanol, after which the pellet was air-dried for 5-10 minutes. The pellet was then
614 resuspended in 200 uL nuclease-free water (Ambion) at 56C, then incubated at 56C with shaking
615 for 30 minutes to resuspend the pure DNA. The sample was centrifuged (12,000 x g, 10 minutes,
616 4C), then the supernatant containing pure DNA was moved to a clean tube. DNA concentration
617 was determined with a NanoDrop spectrophotometer.
618
619 *Digestion of genomic DNA to short oligonucleotides:* 3-5 micrograms of pure genomic DNA was
620 diluted to a 50 uL volume in nuclease-free water, then combined with 50 uL of 2x Dinucleotide
621 Buffer (DB: 5 mU/uL benzonase, 40 mU/uL shrimp alkaline phosphatase, 20 mM Tris pH 7.9, 100
622 mM NaCl, 20 mM MgCl2). Samples were incubated overnight at 37C. Spin-X UF Concentrators
623 (Corning) were rinsed with 200 uL buffer (20 mM Tris pH 7.9, 100 mM NaCl, 20 mM MgCl2), then
624 samples were applied and centrifuged through (12,000 x g, 5 min, RT). The eluate was collected
625 for analysis.
626
627 *Digestion of genomic DNA to mononucleosides:* We extracted mononucleosides from genomic
628 DNA similarly to a previously described method(*47*) with some modifications. 1-3 micrograms of
629 pure genomic DNA was diluted to a 50 uL volume in nuclease-free water, then combined with 50

630 uL of 2x Mononucleoside Buffer (MB: 5 mU/uL benzonase, 40 mU/uL shrimp alkaline
631 phosphatase, 60 uU/uL phosphodiesterase I, 20 mM Tris pH 7.9, 100 mM NaCl, and 20 mM
632 MgCl2). Samples were incubated overnight at 37C. Spin-X UF Concentrators (Corning) were
633 rinsed with 200 uL buffer (20 mM Tris pH 7.9, 100 mM NaCl, 20 mM MgCl2), then samples were
634 applied and centrifuged through (12,000 x g, 5 min, RT). The eluate was collected for analysis.
635
636 **Mononucleoside and Dinucleotide LC-MS/MS**

637 Mononucleoside analyses were carried out by adapting a previously described method(*48*) using
638 a Dionex Ultimate 3000 UHPLC coupled to a Q Exactive Plus mass spectrometer (Thermo
639 Scientific). After purification, analytes were separated on a Hypersil Gold 2.1 x 150 mm column,
640 protected by a 2.1 x 10 mm Hypersil Gold guard column (Thermo Scientific). The mobile phases
641 were A: 0.1% formic acid in water, and B: 0.1% formic acid in acetonitrile. The flow rate was set
642 to 400 µL/min, and the column oven was set to 36°C. 10 µL of each sample was injected, and the
643 analytes were eluted using the following gradient: 0 min- 0% B, 6 min- 0% B, 8.5 min- 80% B, 9.5
644 min- 80% B, 10 min- 0% B, 13 min- 0% B. The Q Exactive Plus was operated in positive mode
645 with a heated electrospray ionization (HESI) source. The spray voltage was set to 3.5 kV, the
646 sheath gas flow rate was set to 40, and the auxiliary gas flow rate set to 7, while the capillary
647 temperature was set to 320°C. A parallel reaction monitoring (PRM) method was used to quantify
648 the unlabeled nucleotide, along with all of its N15 isotopes in a single scan. This was
649 accomplished by using wide (8 m/z) isolation widths when selecting the nucleotides for
650 fragmentation. By employing this method, we were able to quantify the level of labeling by looking
651 at the intensity of each N15 labeled base in the MS2 scan. Fragment ions were detected in the
652 Orbitrap with a resolution of 70,000 at m/z 200. Using a high resolution MS2 scan allowed us to
653 resolve N15 and C13 isotopes. Peak areas from the fragment ions were extracted with a 10 ppm
654 mass tolerance using the LC Quan node of the XCalibur software (Thermo Scientific).

655 Dinucleotide analyses were carried out using the same instrumentation, column, mobile phases,
656 column temperature, and flow rate employed by the mononucleoside experiments. The gradient
657 was changed to optimize dinucleotide separation as follows: 0 min- 5% B, 0.5 min- 5% B, 2.5 min-
658 90% B, 3.25 min- 90% B, 3.5 min- 5% B, 5.5 min- 5% B. The Q Exactive Plus was operated using
659 the same tune settings as the mononucleotide experiment. However, instead of a PRM method,
660 a full scan method from 500-650 m/z was developed to quantify the dinucleotides dCdC, TT,
661 dAdA, and dGdG, along with their corresponding N15 isotopes. Precursor ions were detected in
662 the Orbitrap with a resolution of 140,000 at m/z 200, using the high resolution MS1 scan to try to

663 separate N15 and C13 isotopes as much as possible. Peak areas from the fragment ions were
664 extracted with a 10 ppm mass tolerance using the LC Quan node of the XCalibur software
665 (Thermo Scientific).

666 *Measurement of kdiv*

667 To accurately measure rates of cell division (k_{div}) while factoring in the effects of incomplete
668 labeling and nucleotide recycling, we considered the time-dependent labeling patterns of
669 mononucleosides derived from genomic DNA. Upon initiation of ^{15}N labeling, newly synthesized
670 DNA strands can incorporate nucleotides from a precursor pool that includes fully ^{15}N-labeled
671 nucleotides derived from the dietary source, partially labeled species (containing one to four ^{15}N
672 atoms) derived by biosynthesis from incompletely labeled ^{15}N precursors, and completely
673 unlabeled nucleotides derived from recycling. Therefore, it may not be possible to accurately
674 determine the ratio of new to old strands (and hence k_{div}) from the mononucleotide data alone.
675 We previously used the labeling pattern of dinucleotides to resolve this ambiguity(*14*). The
676 isotopologue distribution of labeled (non-monoisotopic) peaks in the dinucleotide spectra are
677 dependent on the composition of the nucleotide precursor pool. Through regression analyses, we
678 determined that within all tissues and timepoints analyzed in this study, the isotopologue
679 distributions of the dinucleotide data could be best modeled based on the assumption that newly
680 synthesized strands had very low levels of fully unlabeled nucleotides. Hence, the fractional
681 population of labeled non-monoisotopic peaks within dinucleotide and mononucleotide data were
682 consistent with each other and could be used to determine the fractional population of new
683 strands. For each tissue, fractional labeling of mononucleotide and dinucleotides for all 4 bases
684 were combined and the aggregated dataset was fit to a single exponential equation to determine
685 first order rate constant for division (k_{div}). These data appear in Table S2.
686

687 **Analysis of Proteomic Data**

688

689 *Quality filtering and analysis of k_t values:* Proteomic data was acquired in the form of 16-plex TMT
690 replicates containing 2 full 6-timepoint timecourses (one from wild type animals and one from
691 progeroid animals). For each genotype within each TMT replicate, proteins were filtered to retain
692 only those detected with at least 3 peptide spectral matches (PSMs) in all timepoints. Proteins
693 that met these criteria were then filtered per genotype within each TMT replicate based on
694 goodness of fit using the t-statistic. The t-statistic is equal to the turnover rate (k_t) divided by the
695 standard error of that value. This metric determines to what extent measurement error influences

696 k_t. We applied a minimum t-statistic cutoff of 3, meaning that the magnitude of the turnover rate
697 k_t is at least 3 times the magnitude of the standard error. Between 50% to 63% of detected proteins
698 passed these coverage and goodness-of-fit criteria (Figure S2). Along with the sample size, the
699 t-statistic can be used to determine a p-value that indicates the probability that the turnover rate
700 reported has a meaningful non-zero value. The k_t, standard error, t-statistic, and p-value for each
701 protein are reported in Table S1. The k_t, standard error, and sample size were used to perform
702 per-protein statistical tests across tissues, to identify proteins with significantly different turnover
703 kinetics between tissues. These data are reported in Table S1.
704
705 *Determination of relative protein abundance within tissues*: To evaluate relative protein
706 abundance between genotypes within tissues of 3-month-old mice, technical replicate unlabeled
707 wild type and progeroid samples from each multiplexed TMT run were first channel normalized,
708 then the geometric mean was calculated to determine mean normalized intensities for each
709 biological replicate. Protein abundance was then length-normalized by dividing each protein's
710 normalized intensity by the number of amino acids. Finally, samples were normalized for
711 comparison across biological replicates by normalizing each channel to the maximum value
712 detected. The geometric mean abundance across all biological replicates was calculated by
713 determining the geometric mean of the length- and channel-normalized protein abundance.
714 Finally, the fold change of protein abundances between wild type and progeroid tissues was
715 determined.
716
717 Additional multiplexed TMT experiments were performed to compare protein abundances within
718 tissues from 9-month-old wild type and progeroid mice. In these experiments, two biological
719 replicate samples were analyzed in technical duplicate for each genotype in an 8-plex TMT
720 experiment per tissue. Raw data were subjected to the same sequence of technical replicate
721 averaging, protein length normalization, channel normalization, biological replicate averaging,
722 and fold change determination described above.
723
724 *Identification of disease-linked proteins:* Disease associations were determined by cross-
725 referencing proteomic datasets to the Online Mendelian Inheritance in Man (OMIM) database
726 (www.omim.org). A complete list of OMIM allele – gene associations for the mouse genome was
727 downloaded from OMIM, then cross-referenced to mouse proteins in each decile of turnover rate,
728 ranging from 1st decile (most long-lived) to 10th decile (most short-lived) in each tissue. Over-
729 representation of disease alleles in deciles was evaluated by Fisher's exact test.

730

731 **Protein immunoprecipitation from mouse tissues**

732 Metabolically labeled tissue extracts from progeroid animals prepared as described above in PEB
733 for proteomic analysis were used for immunoprecipitation as follows. Approximately 1300-1500
734 ug of lysate (100 uL) was aliquoted into a fresh tube and diluted to 2 mL final volume in Dilution
735 Buffer (10 mM Tris pH 7.4, 150 mM NaCl, 1% Triton-X-100, 1% deoxycholate, 2.5 mM MgCl2,
736 protease and phosphatase inhibitors). For each sampe, 60 uL of Protein G magnetic beads (Life
737 Technologies) were rinsed and resuspended in Dilution Buffer, then added to the diluted lysate.
738 The sample was incubated at 4C with rotation for 30 minutes. Beads were removed and the pre-
739 cleared supernatant was transferred to a clean tube; 5% of the sample was reserved as input. A
740 mixture of two anti-Lamin A/C antibodies was used to immunoprecipitated Lamin A, Lamin C, and
741 Progerin: Lamin A/C E-1 (Santa Cruz sc-376248, 20 uL per IP) and Lamin A/C (Active Motif
742 #39288 Clone 3A6-4C11, 5 uL per IP). The IP was incubated overnight at 4C with nutation. 60 uL
743 of pre-rinsed Protein G beads were then added to the sample and incubated for 30 minutes at 4C
744 with nutation. Beads were collected on a magnetic stand and supernatant (flow-through) was
745 saved in a fresh tube. Beads were washed in 3 x 1 mL of Wash Buffer (10 mM Tris pH 7.4, 150
746 mM NaCl, 0.5 mM EDTA, 0.1% SDS, 1% Triton-X-100, 1% deoxycholate, 2.5 mM MgCl2,
747 protease and phosphatase inhibitors). Following the third wash, liquid was carefully removed
748 using a gel loading tip; 2x SDS-PAGE sample buffer was added to the beads, and proteins were
749 eluted by boiling for 5 minutes at 95C.

750 To check the efficiency of each IP, equal proportions of the input and flow-through
751 fractions were analyzed by Western blotting for Lamin A/C (E-1 HRP, Santa Cruz, sc-376248
752 HRP). If a noticeable decrease in protein abundance was apparent in the flow-through sample,
753 the IP samples were run on an SDS-PAGE gel and stained with Colloidal Coomassie stain. A gel
754 slice containing the Lamin A, Lamin C, and Progerin bands was cut out for downstream mass
755 spectrometry analysis.

756

757 **SIM/PRM-MS of Lamin and Progerin peptides**

758 *Data collection:* SIM/PRM was performed as described above with the following changes. The
759 gradient began at 3% B and held for 2 minutes, increased to 10% B over 5 minutes, increased to
760 38% B over 38 minutes, then ramped up to 90% B in 3 minutes and was held for 3 minutes, before
761 returning to starting conditions in 2 minutes and re-equilibrating for 7 minutes, for a total run time
762 of 60 minutes. The Fusion Lumos was operated using dual experiments, the first being a tSIM

763 scan and the second being a PRM scan. Each tSIM scan targeted ions with an m/z of 597.7463
764 using an isolation window of 20 m/z, covering the range of the unique Progerin peptide and all
765 possible N15 isotopes. The resolution was set to 120,000 at m/z of 200, an AGC target of 1e5,
766 and a maximum injection time of 246 ms. The PRM scan fragmented precursor ions with an m/z
767 of 589.7463 by collision-induced dissociation (CID) using a 1.6 m/z isolation width. The collision
768 energy was set to 30% with a maximum injection time of 250 ms, and an AGC target of 1e4. The
769 Ion Trap Scan Rate was set to 'Rapid'.

770 *Data analysis*: The presence of Progerin was validated using raw MS2 data. Raw SIM data were
771 searched for precursor ions with an m/z of 589.7463 and z of 2 in addition to all possible N15
772 isotopologues. The intensity of each isotopologue was measured using Thermo XCalibur Qual
773 Browser (Table S5).
774

775 **Acknowledgments:** We would like to thank Yana Blokhina, Biao Wang, Esther Paolo Mirasol,
776 Carlos Lizama Valenzuela, and Xi Chen for assistance with tissue dissections; Jonah Cool, Akiko
777 Hata, and David Julius for critical reading of the manuscript; and all members of the Buchwalter
778 lab for encouragement and ideas throughout the project period.
779 **Funding:** We would like to acknowledge the Progeria Research Foundation (A.B.), the Chan
780 Zuckerberg Biohub (A.B.) and the National Institutes of Health (R35 GM119502 and S10
781 OD025242, S.G.) for funding support.
782
783
784 **References**
785

786 1. K. H. Schreiber, B. K. Kennedy, When Lamins Go Bad: Nuclear Structure and Disease. *Cell*.
787 152, 1365–1375 (2013).

788 2. O. Santiago-Fernández, F. G. Osorio, V. Quesada, F. Rodríguez, S. Basso, D. Maeso, L.
789 Rolas, A. Barkaway, S. Nourshargh, A. R. Folgueras, J. M. P. Freije, C. López-Otín,
790 Development of a CRISPR/Cas9-based therapy for Hutchinson–Gilford progeria syndrome. *Nat*
791 *Med*. 25, 423–426 (2019).

792 3. E. Beyret, H.-K. Liao, M. Yamamoto, R. Hernandez-Benitez, Y. Fu, G. Erikson, P. Reddy, J.
793 C. I. Belmonte, Single-dose CRISPR–Cas9 therapy extends lifespan of mice with Hutchinson–
794 Gilford progeria syndrome. *Nature Medicine*, 1–14 (2019).

795 4. L. W. Koblan, M. R. Erdos, C. Wilson, W. A. Cabral, J. M. Levy, Z.-M. Xiong, U. L. Tavarez, L.
796 M. Davison, Y. G. Gete, X. Mao, G. A. Newby, S. P. Doherty, N. Narisu, Q. Sheng, C. Krilow, C.

797 Y. Lin, L. B. Gordon, K. Cao, F. S. Collins, J. D. Brown, D. R. Liu, In vivo base editing rescues
798 Hutchinson– Gilford progeria syndrome in mice. *Nature*, 1–30 (2021).

799 5. F. G. Osorio, C. L. Navarro, J. Cadiñanos, I. C. López-Mejía, P. M. Quirós, C. Bartoli, J.
800 Rivera, J. Tazi, G. Guzmán, I. Varela, D. Depetris, F. de Carlos, J. Cobo, V. Andrés, A. D.
801 Sandre-Giovannoli, J. M. P. Freije, N. Lévy, C. López-Otín, Splicing-directed therapy in a new
802 mouse model of human accelerated aging. *Science translational medicine*. 3, 106ra107-
803 106ra107 (2011).

804 6. M. Puttaraju, M. Jackson, S. Klein, A. Shilo, C. F. Bennett, L. Gordon, F. Rigo, T. Misteli,
805 Systematic screening identifies therapeutic antisense oligonucleotides for Hutchinson–Gilford
806 progeria syndrome. *Nat Med*. 27, 526–535 (2021).

807 7. P. Scaffidi, T. Misteli, Reversal of the cellular phenotype in the premature aging disease
808 Hutchinson-Gilford progeria syndrome. *Nature Medicine*. 11, 440–445 (2005).

809 8. M. R. Erdos, W. A. Cabral, U. L. Tavarez, K. Cao, J. Gvozdenovic-Jeremic, N. Narisu, P. M.
810 Zerfas, S. Crumley, Y. Boku, G. Hanson, D. V. Mourich, R. Kole, M. A. Eckhaus, L. B. Gordon,
811 F. S. Collins, A targeted antisense therapeutic approach for Hutchinson–Gilford progeria
812 syndrome. *Nat Med*. 27, 536–545 (2021).

813 9. O. Santiago-Fernández, F. G. Osorio, V. Quesada, F. Rodríguez, S. Basso, D. Maeso, L.
814 Rolas, A. Barkaway, S. Nourshargh, A. R. Folgueras, J. M. P. Freije, C. López-Otín,
815 Development of a CRISPR/Cas9-based therapy for Hutchinson–Gilford progeria syndrome. *Nat*
816 *Med*. 25, 423–426 (2019).

817 10. J. Swift, I. L. Ivanovska, A. Buxboim, T. Harada, P. C. D. P. Dingal, J. Pinter, J. D.
818 Pajerowski, K. R. Spinler, J.-W. Shin, M. Tewari, F. Rehfeldt, D. W. Speicher, D. E. Discher,
819 Nuclear Lamin-A Scales with Tissue Stiffness and Enhances Matrix-Directed Differentiation.
820 *Science*. 341, 1240104 (2013).

821 11. B. H. Toyama, J. N. Savas, S. K. Park, M. S. Harris, N. T. Ingolia, J. R. Y. III, M. W. Hetzer,
822 Identification of Long-Lived Proteins Reveals Exceptional Stability of Essential Cellular
823 Structures. *Cell*. 154, 971–982 (2013).

824 12. D. Razafsky, C. Ward, C. Potter, W. Zhu, Y. Xue, V. J. Kefalov, L. G. Fong, S. G. Young, D.
825 Hodzic, Lamin B1 and lamin B2 are long-lived proteins with distinct functions in retinal
826 development. *Mol Biol Cell*. 27, 1928–1937 (2016).

827 13. A. Buchwalter, M. W. Hetzer, Nucleolar expansion and elevated protein translation in
828 premature aging. *Nature Communications*, 1–13 (2017).

829 14. J. Hasper, K. Welle, J. Hryhorenko, S. Ghaemmaghami, A. Buchwalter, *Biorxiv*, in press,
830 doi:10.1101/2022.04.24.488979.

831 15. D. Wang, B. Eraslan, T. Wieland, B. Hallström, T. Hopf, D. P. Zolg, J. Zecha, A. Asplund, L.
832 Li, C. Meng, M. Frejno, T. Schmidt, K. Schnatbaum, M. Wilhelm, F. Ponten, M. Uhlen, J.
833 Gagneur, H. Hahne, B. Kuster, A deep proteome and transcriptome abundance atlas of 29
834 healthy human tissues. *Mol Syst Biol*. 15, e8503 (2019).

835 16. B. Schwanhäusser, D. Busse, N. Li, G. Dittmar, J. Schuchhardt, J. Wolf, W. Chen, M.
836 Selbach, Global quantification of mammalian gene expression control. *Nature*. 473, 337–342
837 (2011).

838 17. J. R. Wiśniewski, M. Y. Hein, J. Cox, M. Mann, A "Proteomic Ruler" for Protein Copy
839 Number and Concentration Estimation without Spike-in Standards*. *Mol Cell Proteomics*. 13,
840 3497–3506 (2014).

841 18. J. Swift, I. L. Ivanovska, A. Buxboim, T. Harada, P. C. D. P. Dingal, J. Pinter, J. D.
842 Pajerowski, K. R. Spinler, J.-W. Shin, M. Tewari, F. Rehfeldt, D. W. Speicher, D. E. Discher,
843 Nuclear Lamin-A Scales with Tissue Stiffness and Enhances Matrix-Directed Differentiation.
844 *Science*. 341, 1240104 (2013).

845 19. P. H. Kim, J. Luu, P. Heizer, Y. Tu, T. A. Weston, N. Chen, C. Lim, R. L. Li, P.-Y. Lin, J. C.
846 Y. Dunn, D. Hodzic, S. G. Young, L. G. Fong, Disrupting the LINC complex in smooth muscle
847 cells reduces aortic disease in a mouse model of Hutchinson-Gilford progeria syndrome. *Sci*
848 *Transl Med*. 10, eaat7163 (2018).

849 20. R. Varga, M. Eriksson, M. R. Erdos, M. Olive, I. Harten, F. Kolodgie, B. C. Capell, J. Cheng,
850 D. Faddah, S. Perkins, H. Avallone, H. San, X. Qu, S. Ganesh, L. B. Gordon, R. Virmani, T. N.
851 Wight, E. G. Nabel, F. S. Collins, Progressive vascular smooth muscle cell defects in a mouse
852 model of Hutchinson-Gilford progeria syndrome. *Proceedings of the National Academy of*
853 *Sciences*. 103, 3250–3255 (2006).

854 21. M. R. Hamczyk, R. V. Bellosta, P. Gonzalo, M. J. A. Manzano, P. Nogales, J. F. Bentzon, C.
855 López-Otín, V. Andrés, Vascular Smooth Muscle–Specific Progerin Expression Accelerates
856 Atherosclerosis and Death in a Mouse Model of Hutchinson-Gilford Progeria Syndrome.
857 *Circulation*. 138, 266–282 (2018).

858 22. C. J. Reddel, A. S. Weiss, Lamin A expression levels are unperturbed at the normal and
859 mutant alleles but display partial splice site selection in Hutchinson-Gilford progeria syndrome. *J*
860 *Med Genet*. 41, 715 (2004).

861 23. M. A. D'Angelo, M. Raices, S. H. Panowski, M. W. Hetzer, Age-Dependent Deterioration of
862 Nuclear Pore Complexes Causes a Loss of Nuclear Integrity in Postmitotic Cells. *Cell*. 136,
863 284–295 (2009).

864 24. D. B. McClatchy, M.-Q. Dong, C. C. Wu, J. D. Venable, J. R. Yates, 15N Metabolic Labeling
865 of Mammalian Tissue with Slow Protein Turnover. *J Proteome Res*. 6, 2005–2010 (2007).

866 25. P. Scaffidi, T. Misteli, Lamin A-dependent misregulation of adult stem cells associated with
867 accelerated ageing. *Nature Cell Biology*. 10, 452–459 (2008).

868 26. M. A. Merideth, L. B. Gordon, S. Clauss, V. Sachdev, A. C. M. Smith, M. B. Perry, C. C.
869 Brewer, C. Zalewski, H. J. Kim, B. Solomon, B. P. Brooks, L. H. Gerber, M. L. Turner, D. L.
870 Domingo, T. C. Hart, J. Graf, J. C. Reynolds, A. Gropman, J. A. Yanovski, M. Gerhard-Herman,
871 F. S. Collins, E. G. Nabel, R. O. Cannon, W. A. Gahl, W. J. Introne, Phenotype and course of
872 Hutchinson-Gilford progeria syndrome. *The New England journal of medicine*. 358, 592–604
873 (2008).

874 27. K. Ben-Harush, N. Wiesel, D. Frenkiel-Krispin, D. Moeller, E. Soreq, U. Aebi, H. Herrmann,
875 Y. Gruenbaum, O. Medalia, The Supramolecular Organization of the C. elegans Nuclear Lamin
876 Filament. *J Mol Biol*. 386, 1392–1402 (2009).

877 28. K. T. Sapra, Z. Qin, A. Dubrovsky-Gaupp, U. Aebi, D. J. Müller, M. J. Buehler, O. Medalia,
878 Nonlinear mechanics of lamin filaments and the meshwork topology build an emergent nuclear
879 lamina. *Nat Commun*. 11, 6205 (2020).

880 29. J. Swift, I. L. Ivanovska, A. Buxboim, T. Harada, P. C. D. P. Dingal, J. Pinter, J. D.
881 Pajerowski, K. R. Spinler, J.-W. Shin, M. Tewari, F. Rehfeldt, D. W. Speicher, D. E. Discher,
882 Nuclear Lamin-A Scales with Tissue Stiffness and Enhances Matrix-Directed Differentiation.
883 *Science*. 341, 1240104 (2013).

884 30. B. Nmezi, J. Xu, R. Fu, T. J. Armiger, G. Rodriguez-Bey, J. S. Powell, H. Ma, M. Sullivan, Y.
885 Tu, N. Y. Chen, S. G. Young, D. B. Stolz, K. N. Dahl, Y. Liu, Q. S. Padiath, Concentric
886 organization of A- and B-type lamins predicts their distinct roles in the spatial organization and
887 stability of the nuclear lamina. *Proc National Acad Sci*. 116, 201810070 (2019).

888 31. M. Eriksson, W. T. Brown, L. B. Gordon, M. W. Glynn, J. Singer, L. Scott, M. R. Erdos, C. M.
889 Robbins, T. Y. Moses, P. Berglund, A. Dutra, E. Pak, S. Durkin, A. B. Csoka, M. Boehnke, T. W.
890 Glover, F. S. Collins, Recurrent de novo point mutations in lamin A cause Hutchinson-Gilford
891 progeria syndrome. *Nature*. 423, 293–298 (2003).

892 32. B. Burke, C. L. Stewart, The nuclear lamins: flexibility in function. *Nature Publishing Group*.
893 14, 13–24 (2012).

894 33. A. C. Peterson, J. D. Russell, D. J. Bailey, M. S. Westphall, J. J. Coon, Parallel Reaction
895 Monitoring for High Resolution and High Mass Accuracy Quantitative, Targeted Proteomics*.
896 *Mol Cell Proteomics*. 11, 1475–1488 (2012).

897 34. G. C. McAlister, E. L. Huttlin, W. Haas, L. Ting, M. P. Jedrychowski, J. C. Rogers, K. Kuhn,
898 I. Pike, R. A. Grothe, J. D. Blethrow, S. P. Gygi, Increasing the Multiplexing Capacity of TMTs
899 Using Reporter Ion Isotopologues with Isobaric Masses. *Anal Chem*. 84, 7469–7478 (2012).

900 35. P. Ciryam, G. G. Tartaglia, R. I. Morimoto, C. M. Dobson, M. Vendruscolo, Widespread
901 Aggregation and Neurodegenerative Diseases Are Associated with Supersaturated Proteins.
902 *Cell Reports*. 5, 781–790 (2013).

903 36. H. Olzscha, S. M. Schermann, A. C. Woerner, S. Pinkert, M. H. Hecht, G. G. Tartaglia, M.
904 Vendruscolo, M. Hayer-Hartl, F. U. Hartl, R. M. Vabulas, Amyloid-like Aggregates Sequester
905 Numerous Metastable Proteins with Essential Cellular Functions. *Cell*. 144, 67–78 (2011).

906 37. J. Hasper, K. Welle, J. Hryhorenko, S. Ghaemmaghami, A. Buchwalter, *Biorxiv*, in press,
907 doi:10.1101/2022.04.24.488979.

908 38. J. A. M. Bard, C. Bashore, K. C. Dong, A. Martin, The 26S Proteasome Utilizes a Kinetic
909 Gateway to Prioritize Substrate Degradation. *Cell*. 177, 286-298.e15 (2019).

910 39. N. F. Bence, R. M. Sampat, R. R. Kopito, Impairment of the Ubiquitin-Proteasome System
911 by Protein Aggregation. *Science*. 292, 1552–1555 (2001).

912 40. J. Rivera-Torres, R. Acín-Perez, P. Cabezas-Sánchez, F. G. Osorio, C. Gonzalez-Gómez,
913 D. Megias, C. Cámara, C. López-Otín, J. A. Enríquez, J. L. Luque-García, V. Andrés,
914 Identification of mitochondrial dysfunction in Hutchinson–Gilford progeria syndrome through use
915 of stable isotope labeling with amino acids in cell culture. *Journal of Proteomics*. 91, 466–477
916 (2013).

917 41. P. Scaffidi, T. Misteli, Lamin A-dependent nuclear defects in human aging. *Science*. 312,
918 1059–1063 (2006).

919 42. K. Cao, B. C. Capell, M. R. Erdos, K. Djabali, F. S. Collins, A lamin A protein isoform
920 overexpressed in Hutchinson–Gilford progeria syndrome interferes with mitosis in progeria and
921 normal cells. *Proc National Acad Sci*. 104, 4949–4954 (2007).

922 43. D. Gabriel, D. Roedl, L. B. Gordon, K. Djabali, Sulforaphane enhances progerin clearance in
923 Hutchinson-Gilford progeria fibroblasts. *Aging Cell*. 14, 78–91 (2014).

924 44. B. J. Hindson, K. D. Ness, D. A. Masquelier, P. Belgrader, N. J. Heredia, A. J. Makarewicz,
925 I. J. Bright, M. Y. Lucero, A. L. Hiddessen, T. C. Legler, T. K. Kitano, M. R. Hodel, J. F.
926 Petersen, P. W. Wyatt, E. R. Steenblock, P. H. Shah, L. J. Bousse, C. B. Troup, J. C. Mellen, D.
927 K. Wittmann, N. G. Erndt, T. H. Cauley, R. T. Koehler, A. P. So, S. Dube, K. A. Rose, L.
928 Montesclaros, S. Wang, D. P. Stumbo, S. P. Hodges, S. Romine, F. P. Milanovich, H. E. White,
929 J. F. Regan, G. A. Karlin-Neumann, C. M. Hindson, S. Saxonov, B. W. Colston, High-
930 Throughput Droplet Digital PCR System for Absolute Quantitation of DNA Copy Number. *Anal*
931 *Chem*. 83, 8604–8610 (2011).

932 45. G. C. McAlister, D. P. Nusinow, M. P. Jedrychowski, M. Wühr, E. L. Huttlin, B. K. Erickson,
933 R. Rad, W. Haas, S. P. Gygi, MultiNotch MS3 Enables Accurate, Sensitive, and Multiplexed
934 Detection of Differential Expression across Cancer Cell Line Proteomes. *Anal Chem*. 86, 7150–
935 7158 (2014).

936 46. K. A. Welle, T. Zhang, J. R. Hryhorenko, S. Shen, J. Qu, S. Ghaemmaghami, Time-resolved
937 Analysis of Proteome Dynamics by Tandem Mass Tags and Stable Isotope Labeling in Cell
938 Culture (TMT-SILAC) Hyperplexing*. *Mol Cell Proteomics*. 15, 3551–3563 (2016).

939 47. E. P. Quinlivan, J. F. G. III, DNA digestion to deoxyribonucleoside: A simplified one-step
940 procedure. *Analytical Biochemistry*. 373, 383–385 (2008).

941 48. D. Su, C. T. Y. Chan, C. Gu, K. S. Lim, Y. H. Chionh, M. E. McBee, B. S. Russell, I. R.
942 Babu, T. J. Begley, P. C. Dedon, Quantitative analysis of ribonucleoside modifications in tRNA
943 by HPLC-coupled mass spectrometry. *Nat Protoc*. 9, 828–841 (2014).

944

945

946

947

Data and Materials availability: LC-MS/MS data have been deposited in the ProteomeXchange Consortium via the PRIDE partner repository, accessible at www.ebi.ac.uk/pride. The accession codes will be included in the final manuscript.

Supplementary Materials

Materials and Methods

Figs. S1 to S6

Tables S1 to S5